ACCESS
Arctic Climate Change
Economy and Society

Project no. 265863

ACCESS

Arctic Climate Change, Economy and Society

Instrument: Collaborative Project

Thematic Priority: Ocean.2010-1 "Quantification of climate change impacts on economic sectors in the Arctic"

D4.4.2 – Assessment of the behaviour of different types of oil and gas products in a cold water environment based on experiments and modelling

Due date of deliverable: **31/08/2013**

Actual submission date: **16/02/2015**

Start date of project: **March 1st, 2011** Duration: **48 months**

Organisation name of lead contractor for this deliverable: **SAMS/BAS**

Project co-funded by the European Commission within the Seventh Framework Programme (2007-2013)		
Dissemination Level		
PU	Public	X
PP	Restricted to other programme participants (including the Commission Services)	
RE	Restricted to a group specified by the consortium (including the Commission Services)	
CO	Confidential, only for members of the consortium (including the Commission Services)	

D4.4.2 – Assessment of the behaviour of different types of oil and gas products in a cold water environment based on experiments and modelling

By

Jeremy Wilkinson

British Antarctic Survey /Scottish Association for Marine Science

CJ.Beegle-Krause

SINTEF

Karl Ulrich-Evers

Hamburgische Schiffbau-Versuchsanstalt (HSVA)

Nick Hughes, Penny Wagner

Norwegian Meteorological Institute

Peter Wadhams

University of Cambridge

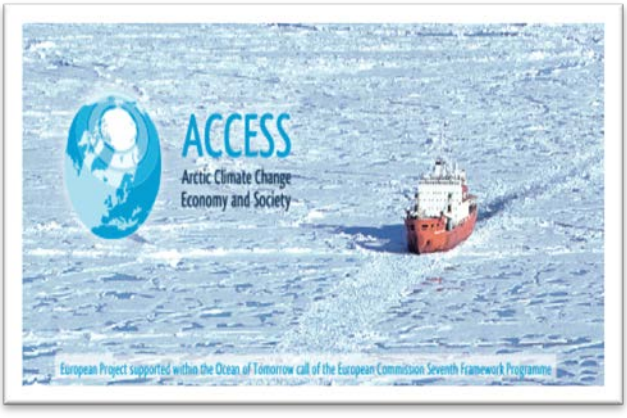

ACCESS is a 4 year European program (2011-2015) supported within the Oceans of Tomorrow call of the European Commission Seventh Framework Programme.

For further information about ACCESS please visit our website at www.access-eu-org

Table of contents

1. Introduction

The behaviour of different types of oil products in a cold water environment can be thought of as a function of three variables (1) the oil properties (i.e. viscosity, density, interfacial tension etc.), (2) the characteristics of the spill (i.e. spill duration, flow rate etc.) and (3) the environmental parameters (i.e. oceanic, sea ice and atmospheric properties) at the time.

We all are well aware that when oil is spilled on the ocean's surface it spreads outwards to form a slick. The extent of the slick is the balance between the amount of oil (i.e. the hydrostatic pressure), and the forces of gravity, viscosity and surface-tension. It is also worth noting that the trajectory or drift of the slick is predominately governed by the environmental forces such as currents, winds and waves (Wang et al., 2005).

Similar forces act on the movement of oil spilled under sea ice, however the importance of the different parameters varies significantly. This can be clearly seen in the difference in the equilibrium thickness of oil spilled on the sea surface and oil spilled under sea ice.

On the sea surface the equilibrium oil thickness is in the range of micrometres to millimetres (varies with the oil properties). Because of this tight range the Bonn Agreement (2004) has developed five levels of oil appearance/thickness code levels. These are:

Code	Appearance	Layer Thickness Interval (µm)	Litres per square km (l/km^2)
1	Sheen (silvery/grey)	0.04 to 0.30	40 – 300
2	Rainbow	0.30 to 5.0	300 – 5000
3	Metallic	5.0 to 50	5000 – 50,000
4	Discontinuous True Oil Colour	50 to 200	50,000 – 200,000
5	Continuous True Oil Colour	200 to More than 200	200,000 - More than 200,000

This code system in not appropriate for oil under sea ice as experiments suggest that the equilibrium thickness of an oil lens under sea ice is much thicker. For example on a perfectly smooth and level ice surface the oil will form droplets, lenses or slicks whose thickness depends on the balance of surface tension versus

buoyancy forces around the rim of the lens. If the lens is of large diameter its thickness H is given by

$$H^2 \, \partial\rho \, g = 2 \, T \, (1 - \cos \theta) \qquad (1)$$

Where $\partial\rho$ is density difference between oil and seawater, T is surface tension at the oil-ice interface and θ is the oil/ice contact angle measured within the oil.

During the Beaufort Sea Project in Canada in the 1970s Norman Wells crude oil was used as a surrogate for Beaufort Sea crude. It had physical properties which when applied to equation (1) yielded H = 0.55 to 0.68 cm, in good agreement with the thickness of slicks observed by divers when Norman Wells crude was spilled under moving pack ice (Dickins et al., 1975). In laboratory tests most types of crude had H in the range 0.5 to 1 cm (Keevil and Ramseier, 1975). A slightly thicker equilibrium thickness of about 2 cm was suggested by Kovacs et al., (1981), whilst Greene et al., (1977) found a minimum thickness of between 0.5 and 2 cm. If we assume a spreading thickness of between 0.5 and 2 cm we see that under smooth ice oil will hold between 500,000 litres per km^2 and 2,000,000 litres per km^2.

As we will see in this report the underside of sea ice is not smooth, there are irregular undulations on the bottom of the ice due to spatial variations in snow loading (Wadhams and Martin, 1990; Wadhams et al., 2006). Snow acts as an insulator, reducing the heat exchange between the atmosphere and ice-ocean interface, thus reducing the thermodynamic growth in regions with a thicker snow cover. Further irregularities on the ice bottom are due to the mechanical deformation of sea ice (ridges and leads), the differential melt processes in summer (i.e. melt ponds). These under-ice topographic feaures can provide effective catchments to contain any spilled oil (Barnes et al., 1979; Kovacs et al., 1981).

This report summarises our knowledge on the behaviour of oil under sea ice, as well as advancing this knowledge through dedicated experiments. First we provide a review of the sea ice properties and its unique under ice topography, then we discuss the oil properties, and finally present results from our experiments.

2. Sea ice morphology

Once the surface of the ocean is cooled to its salinity determined freezing point any additional heat loss produces a slight super-cooling of the water after which the formation of loose crystals known as frazil ice occurs. If both the wave and wind effects are reduced the agitation of the frazil ceases and the surface layer of frazil crystals can preferentially fuse together to form a level, thin ice cover known as nilas. This is cycle is known as the frazil-nilas-ice sheet cycle. Further thickening will then occur by freezing of seawater on the underside of the ice. This downward growth process is known as congelation growth and, barring mechanical deformation of the ice sheet, the ice will form a relatively level, uniform ice sheet. Due to spatial variability of ice properties and snow cover there will invariably be some small-scale variability in ice thickness, even for very uniform ice.

However, if some kind of turbulence within the upper surface layer of a body of water persists (i.e. generated by wind, wave or current), then a different ice formation scenario occurs. This turbulence promotes a specific ice development process as the waves or swell inhibit the formation of large sheets of nilas, but do allow the frazil crystals agglomerate into small clumps. As these grow through continued freezing of frazil, they are buffeted by waves and contact with other ice clumps, so that they form small rounded pans, or “pancake ice”. As the wave energy is damped by the ice, the pancakes will begin to freeze together, eventually forming a consolidated sheet. Further thickening will occur via congelation growth on the ice bottom. This is known as the frazil-pancake-ice sheet cycle. A graphical description can be seen in figure 1.

Once a continuous ice sheet is formed it is collectively known as first year ice (FY). FY ice formed at the start of the winter will be between 1 and 2 m thick by the start of the following melt season, and be relatively smooth in appearance. FY ice that survives the summer melt then becomes known as Multiyear ice (MY). MY ice can be many years old, is generally thick, and can be heavily deformed.

It is important to remember that sea ice is in a constant state of flux, due to changing atmospheric and, to a lesser extent, oceanographic conditions. Not only

does the sea ice increase and decrease in thickness with the seasons (thermodynamic growth and melt processes), but mechanical redistribution of sea ice is common. Idiosyncrasies in the drift of sea ice allows the ice to be jammed together to form ridges, or is forced apart to form leads..

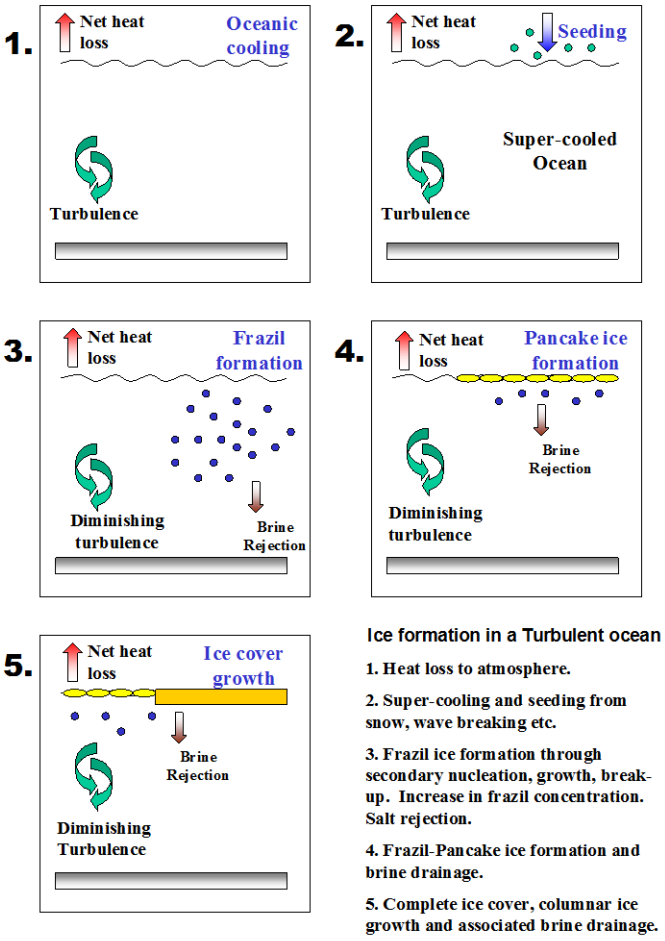

Figure 1 Visual illustration showing the processes of ice formation within a turbulent ocean.

All these changes in the morphology of the sea ice are reflected in the underside ice topography i.e. the bottom of FY ice is regarded as smooth whereas MY ice is quite rugged as a result of the differential melt/growth rates throughout the seasons (Wadhams, 1985). Knowledge of the under-ice topography is important because it is fundamental in determining both the volume of oil that can be held by the ice (the pooling capacity), as well as the direction of flow of the oil. Therefore a first step in evaluating the behaviour of oil under sea ice is an accurate knowledge of bottom topography of different ice types, but his is more difficult that it sounds.

Over the years a number of *in-situ* techniques have been utilised to obtain information on sea ice thickness and the shape of the ice underside. These include electromagnetics, ground penetrating radar, altimetry, electromagnetic, and drilling. A summary of these and other techniques can be found in Wadhams (2000). These methods provide only a low-resolution picture of the sea ice bottom topography. For example In the 1970s and 1980s a limited number of experiments were performed to quantify the pooling capability of a potential oil spill under undeformed fast ice. These experiments were aimed at obtaining the 3-dimensional underside relief of the ice through a gridded drilling (Barnes et al., 1979) and ground penetrating radar programme (Kovacs, 1977; Kovacs et al., 1981). These gridded surveys, of about 200 m in length, only provide a very coarse snapshot of the underside. This is because the spatial distribution of the sampling means that the richness of the three-dimensional (3-D) structure of sea ice is lost. Consequently we did not have the data to replicate the complexity or uniqueness of various ice regimes.

The use of sonars to image the underside of ice has been performed for many decades (see Wilkinson et al., 2007 and refs within). The first under-ice surveys used single beam sonars to produce two-dimensional profiles (thickness and distance travelled) of the under ice topography. Now, multibeam sonars are capable of imaging the full three-dimensional topography of the sea ice underside at high resolution (a few cm vertically, and better than 20 cm horizontally depending on the proximity to the ice).

A major advance in visualising (at high-resolution) the 3-D nature of the underside of sea ice was realised through the incorporation of an upward-looking multibeam sonar onto Autonomous Underwater Vehicles (AUVs). This pioneering concept showed in unprecedented detail the 3-D nature of the under-ice surface (Wadhams et al., 2006). An example can be seen in Figure 2. To obtain the same resolution through a drilling programme over 1.5 million holes would have to be drilled, an impossible task.

Figure 2 it a great example of the complexity of the underside of first year ice. For example we can see both areas of level ice (light blue regions) as well as regions of deformed ice (red). However we must remember that this example represents a

snap-shot in time and space of just one ice type; first year ice. The examples in Figure two represent data from a single track from an upward-looking swath mapping sonar mounted on an Autonomous Under water Vehicle (AUV) with an upward looking swath mapping sonar. During this experiment data was collected during 14 overlapping legs. These legs were then stitched together to form a larger mosaic. In the following sections we discuss the origin and under ice topography of different ice types that may be encountered should an oil spill occur in ice invested waters.

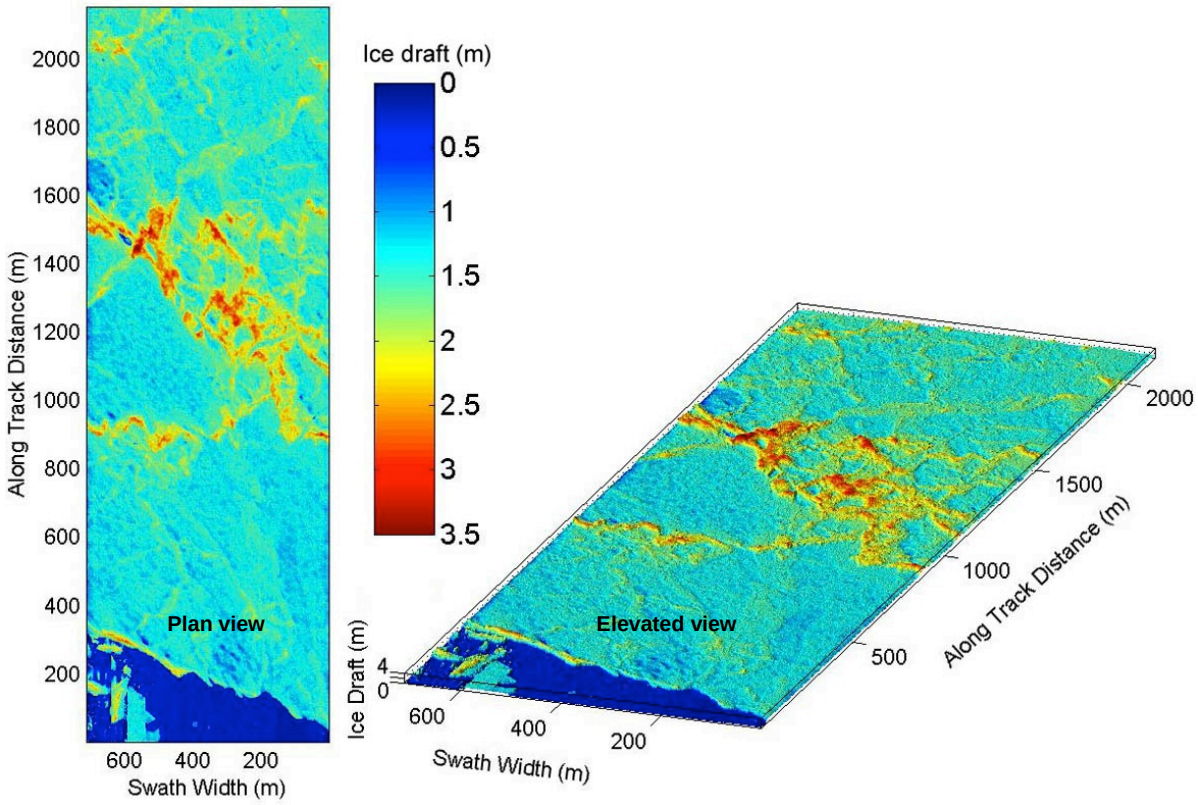

Figure 2. 3-D imagery of the underside of sea ice obtained from an AUV mounted multibeam sonar mounted. This mosaic was constructed from 14 overlapping survey runs. The influence of under ice features have on the flow of oil can be seen i.e. a ridge system. This data represents the highest quality 3-D under-ice topography data presently available.

2.1 Under ice topography of different ice types.

As the Arctic transitions to a seasonal ice cover (possibly within the next few decades), larger areas of open water will be present at the end of summer. These regions of open water will persist for longer periods of time, thus allowing an

extended window of operation for shipping, fisheries, tourism and hydrocarbon exploration. Given this knowledge it is likely, for the foreseeable future, that shipping and exploration for hydrocarbons in the Arctic is likely to occur during the summer open-water period or extending into the freeze up period. if freeze-up occurs particularly early, there is the possibility these operations may occur within a field of new ice, i.e. frazil, nilas, or pancake ice.

Furthermore the dynamic nature of sea ice means that it can be found many hundreds of kilometres away from the main ice edge. As a result moving platforms (i.e. ships) or fixed assets (such as drilling platforms) may come in contact with older ice types i.e. individual floes or fields of first-year and multi-year floes at any stage of the summer season.

As mentioned previously the rate and direction at which oil spreads under ice is determined by a combination of factors, but it is the under-ice topography that is fundamental in determining both the volume of oil that can be held by sea ice (its oil pooling capacity) and the direction of flow. Therefore a first step in understanding and evaluating the dispersal of oil under sea ice must be an accurate knowledge of its bottom topography.

The mounting of a multibeam sonar on an autonomous underwater vehicle was a huge leap forward for under-ice studies, especially in our understanding of the shape of sea ice. By doing so a mechanism to record, in unprecedented detail, the three-dimensional nature of the under-ice surface was available. Within WP 1 of ACCESS and other funded programmes we are beginning to develop a library of information on the shape of the underside of different types of sea ice.

Within this section we show examples of the under ice topography of different ice types. These include: frazil, nilas, pancake, as well as level and deformed first year and multiyear ice.

2.1.1 Frazil Ice

As mentioned previously frazil ice is the first stage of sea ice formation (figure 3). The size of frazil crystals range from 0.05 to several millimetres in fresh water (Daly and Colbeck, 1986), and 1 to 10 millimetres in sea water (Weeks, 1998). As long as

heat is being removed at a rate greater than that introduced to the system by the latent heat of fusion released during ice formation, frazil will continue to be formed. Within the laboratory, rates of frazil production have been shown to be 30 to 100 times greater in the presence of turbulence than when quiescent conditions prevail (Voropayev et al. 1995). Field observations by Reimnitz and Kempema (1987) indicate that large volumes of frazil are produced when winds of at least 10 ms^{-1} are associated with temperatures of -10°C or colder.

Figure 3 Newly formed frazil crystals and clumps of frazil on the ocean surface. These crystals dampen down the high frequency end of the incoming wave spectra and hence are sometimes collectively referred to as grease ice. The dark areas in the foreground are patches of open water. The white shapes within the frazil are very small pancakes.

Under strong wind conditions the frazil layer can develop to a considerable thickness. For example Reimnitz and Kempema (1987) witnessed a frazil several metres in thickness in the Barents Sea. Despite the common nature of this ice type there is very little information known about the underside nature of frazil ice.

To date the author is not aware of 3-D imagery relating to the shape of the underside of a frazil ice layer. An example of a side scan image of the underside of sea ice can be seen in figure 4 (Wadhams *et al.*, 2004). This figure shows a series of first year ice floes (notice the smooth nature of the ice bottom) surrounded by frazil ice. From this image it looks like the bottom of the frazil is relatively smooth.

However, it should be stressed that side scan sonar produces a qualitative 2-dimensional 'photographic' image with no quantitative information on ice thickness/draft.

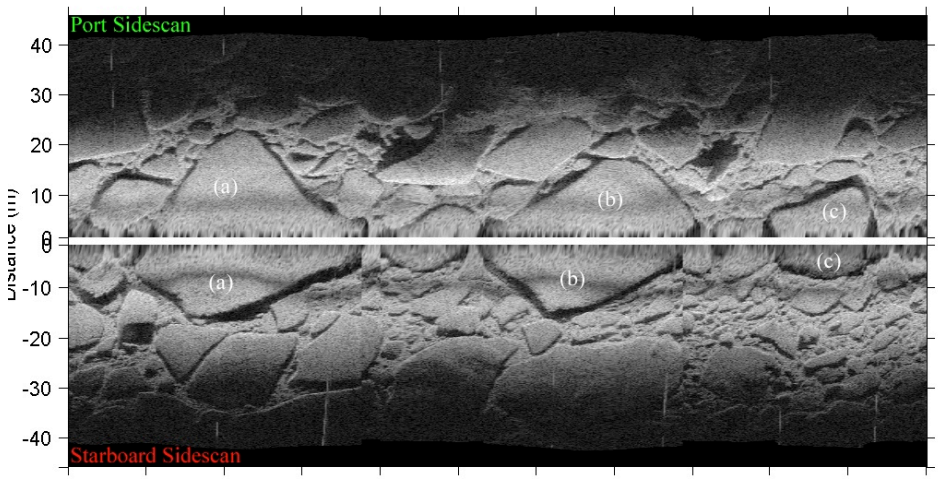

Figure 4 An example of upward looking sidescan from showing a high concentration of frazil surrounding ice floes. Three angular multi-year floes (labelled (a), (b) and (c)), each up to 2.5 m thick and be seen in the central region of the image. No open water is visible in the image (Wadhams et al., 2004).

2.1.2. Nilas

If both the wave and wind effects are reduced the agitation of the frazil ceases and the surface layer of frazil can begin to consolidate. Furthermore the upper frazil layers also have a greater propensity for heat loss because they are exposed to the cold atmosphere. This in turn enables them to grow, and fuse to form nilas. Nilas is observed to be extremely plastic and can easily bend to accommodate a small incoming wave field. The transformation of frazil to nilas can occur within several hours (Zubov, 1945) and within 48 hours it may support the weight of a man (Scoresby, 1815). Further thickening will continue as a unidirectional process by which seawater freezes directly to the underside as heat is conducted through the ice. This is known as congelation growth. This is the start of sea ice forming a continuous, thick sheet.

As with frazil there is very little information known about the underside topography of nilas, however is suspected to be relatively smooth. Although given the thin nature of nilas it is very susceptible to rafting and fingering.

2.1.3. Pancake ice

If the wind decreases but the swell persists, frazil will continue to be agitated. Under the influence of the motion of the waves this newly formed crust of ice does not form a continuous sheet but is broken into small rounded pancake shaped pieces normally a few tens of centimetres in diameter (figure 5 and 6). The diameter of primary pancakes depends on the high-frequency part of the wave spectrum (Leonard et al, 1999). Newly formed pancakes are very weak and will easily break into their frazil components if forced. However as time passes, and sub-freezing air temperatures persist, the interstitial water between frazil crystals freeze together.

Figure 5. Young pancake ice. Notice the flat central surfaces carry a thin film of sea water. Their dark colour suggests the internal structure of the pancake is saturated with sea water and hence have very little internal strength. The raised edges are due to the collisions between pancakes as well as the lifting of frazil onto the pancakes by waves. Frazil ice surrounds the pancakes.

Figure 6. Mature pancake field. The darkish colour of the pancakes has disappeared and is replaced by a white, dry snow cover. These robust pancakes still have the raised rims that defines pancake ice. Frazil ice surrounds the pancakes. A metre measuring stick can be seen in the lower left hand corner of the image.

Around the circumference of pancake ice is a raised ridge initially 1 or 2 cm higher than the surrounding plane of the pancake. These rims are formed by the piling of frazil ice around the edges of the pancakes by the general jostling and collisions between pancakes and the cyclic pressure pulses of the wave field. Once the incoming wave energy has decayed sufficiently pancakes will freeze together, with the frazil acting as the adhesive, to form an extensive sheet.

The exact distance from the ice edge before pancakes freeze together varies depending on the incoming wave spectra. However if the penetrating wave energy increases again the newly formed ice sheet may be broken into floes, the size of which will be determined by the incoming wave spectra. Between the floes will be a combination of smashed floes of varying sizes and newly formed frazil. When the wave energy decreases sufficiently this mixture will freeze together with the floes to form a new ice sheet. This process can occur repeatedly during freeze-up.

As with frazil ice we are not aware of any of 3-D imagery relating to the shape of the underside of pancake ice. However we do have access to results from the in situ sampling of pancake ice (figure 7 and 8).

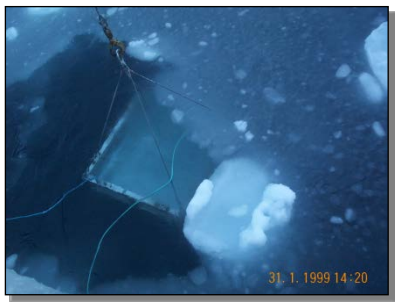

Figure 7a. Luring the pancake into the catcher

Figure 7b. Caught…

Figure 7c. Bringing pancake aboard for analysis.

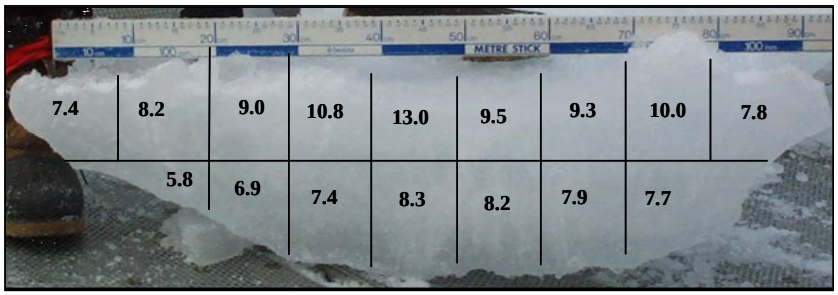

Figure 8. Typical side view profile of a mature pancake. The salinity of different sections of the pancake are overlaid on the image.

From these results we can see that the bottom of individual pancakes are bowl-like. Therefore we can expect the under ice topography of a field of pancakes to consist of many bowl-like features, producing a very undulating bottom topography.

2.1.4 First year ice

First year (FY) ice is the nomenclature used to describe ice floes that are less than a year old. Sea ice that started to grow at the commencement of winter is usually reaches a thickness of 1-2 m by the following summer. FY ice generally has a smooth appearance, but due to dynamic nature of sea ice ridges and not uncommon. Even under smooth FY ice there are irregular undulations on the bottom of the ice due to spatial variations in snow loading (Wadhams and Martin, 1990; Wadhams et al., 2000). Snow acts as an insulator, reducing the heat exchange between the atmosphere and ice-ocean interface, thus reducing the thermodynamic growth in regions with a thicker snow cover.

2.1.5 MultiYear ice

FY ice that survives the summer melt then becomes MY ice. It is generally thick and can be highly deformed ice. In winter snow is blown across it and is collected by the rough surface of the ridges and hummocks and helps to give a more undulating shape to the surface topography. In summer the snow and ice melts and melt pond formation is common, ridges and hummocks become smaller and more rounded due to the melting. Due to the changing climate MY ice is becoming less common ice type in the Arctic (Kwok, 2008). With respect to its morphology the underside of MY ice is quite rugged. This is a result of the differential melt and growth rates throughout the seasons (Wadhams, 1985).

2.1.6. Undeformed First year and Multiyear ice

Figure 9 displays the underside of thermodynamically grown first year ice (on right) and multiyear ice (on left). Even though there is the difference in the thickness of these ice types, around 2 m for MY ice and 1 m for FY ice is expected, the difference in roughness is surprising. The small-scale deviations in roughness of around 0.1m in the FY ice are most likely due to difference in the snow depths on the sea ice. The MY ice has large pockmarks on the underside of the ice. These pockmarks are quite deep, in some instances extending to the near surface of the ice, and are most likely relate to surface melt pond features.

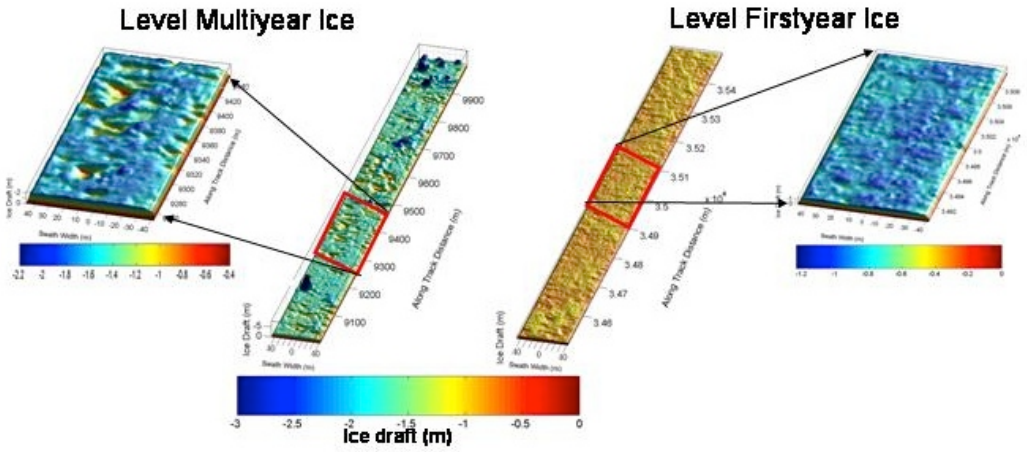

Fig 9 Subset from the multibeam record showing the 3-dimensional detail of the underside first year fast ice and multiyear ice.

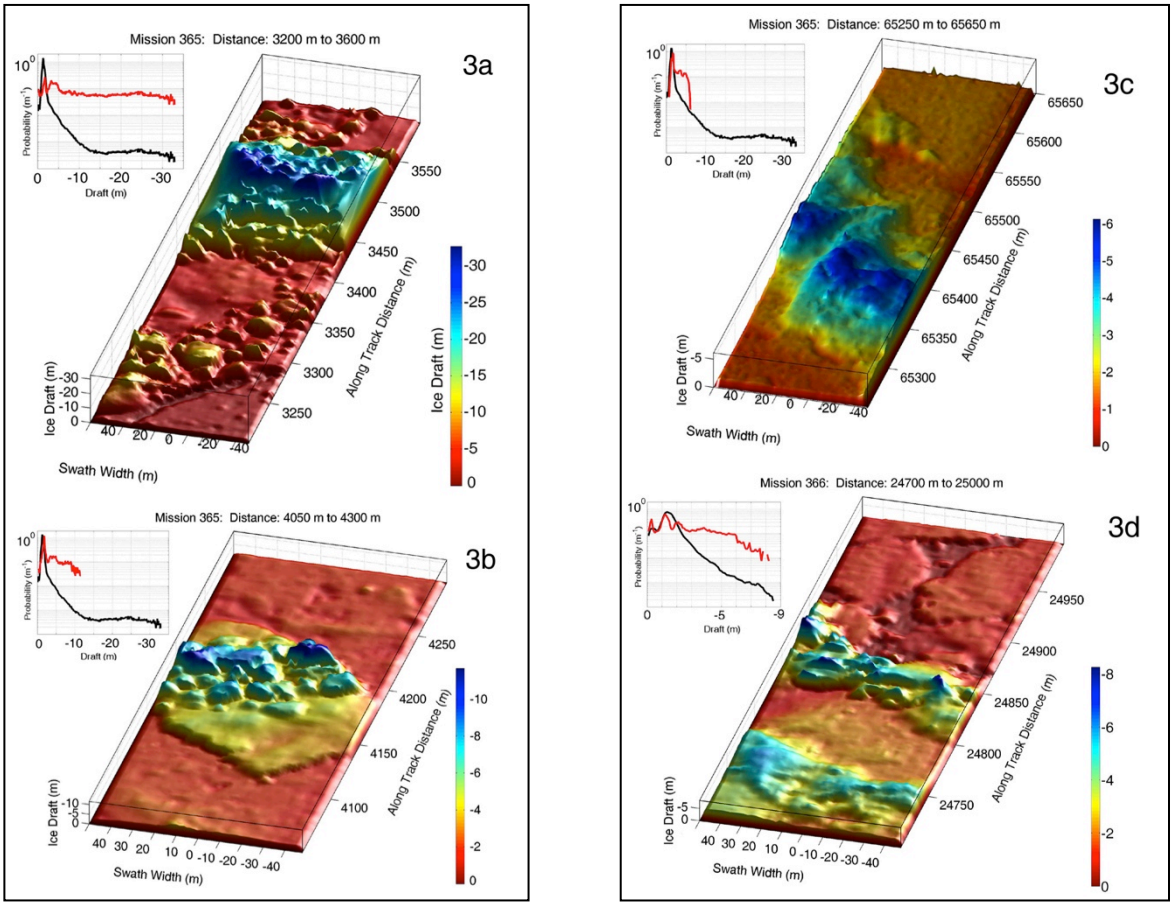

Figure 10 (a) Deep rpressure ridge (>30 m)
(b) MY floe embedded within FY ice
(c) Ridge showing fracture zone
(d) Refrozen broken floes

From Wadhams et al., 2006

2.1.7 Deformed First year and Multiyear ice

When sea ice comes under compression the catastrophic failure of the ice may occur. This can form feature such as ridges or rubble fields. No two of these features are the same, but they are all made up of a disorderly collection of ice blocks. A selection of multibeam imagery of these features can be seen in figure 10.

2.1.8 Summary:

The spread of oil under sea ice is very different to that on the sea surface. For example it will not be influenced by the wind directly, but will preferentially flow along the ice bottom towards regions of thinner ice, accumulating in interconnected depressions under the ice as it spreads. Because of this characteristic under-ice roughness dominates the oil's behaviour. We have shown that different sea ice types have different under ice topographies, which in turn will influence the behaviour of oil. At present we an incomplete understanding of the spread of oil under most ice types and ridges, but advances are being made as we show in Section 4.

3. Oil types and Properties

Crude oil varies widely in its physical and chemical properties, but as the crude is refined the resultant petrochemicals products become more well-defined, although the properties of residual products such as intermediate and heavy fuel oils can vary considerably. The main physical properties of crude oil can be divided into six areas. These are:

i. Specific gravity/Density: Is the relative density of oil in relation to pure water. Most oils have a specific gravity 0.8 gcm^{-3} and thus are lighter than sea ice that has a density of around 0.9 gcm^{-3}, and seawater that has a specific gravity of around 1.025 gcm^{-3}. Therefore fresh oil will rise to the sea or ice surface if it can. Furthermore the density can often give a general indication of other properties, for example oils with low densities tend to contain a high proportion of volatile components and generally have a low viscosity.

ii. Wax content: Oils with a wax content greater than about 10% tend to have high pour points. High wax contents also help to stabilize water-in-oil emulsions. Some light oils behave more like heavy oils due to relatively high wax content.

iii. Pour point: The temperature below which an oil will not flow. If the ambient temperature is below the pour point the oil will be solid-like and not spread over the sea surface as a film.

iv. Distillation characteristics: As the temperature of the oil is raised different components reach their boiling points and are distilled off. This determines the volatility of an oil and controls the rate and extent of evaporation. The distillation characteristics are displayed as percentage volumes that distil off within set temperature ranges.

v. Asphaltene content: Asphaltenes are tar-like substances that enable oil to form a water-in-oil emulsion. Oils with asphaltene contents greater than 0.5% tend to form stable emulsions. These emulsions can contain up to 80% water by volume and are generally extremely viscous.

vi. Viscosity: The viscosity of an oil is its resistance to flow. High viscosity oil flows with difficulty, while oil with low viscosities are highly mobile and spread quickly over the sea surface. It is important to remember that the viscosity of oil increases as temperature decreases and therefore sea and air temperatures are important in determining the viscosity of an oil spill.

With respect to the movement of oil under sea ice it is the density and viscosity of the oil that plays a major role. In is important to note that weathering processes (not covered in this report) will alter the properties of the oil.

3.1 Density of Crude Oils

On the most basic level raw crude oil is classified by the geographic region from which it was extracted i.e. Alaskan North Slope or Saudi Arabia Medium. However, the physical and chemical properties of oil from a particular region can vary significantly and therefore further classification is needed, for example the density of the oil product.

In fact density is one of the most important properties of a crude oil as it has a strong bearing on its value i.e. lighter crudes are preferred to heavier crudes as they are more usable by society i.e. take petrol for example. Interestingly the Industry uses American Petroleum Institute (API) Gravity rather than the actual density when describing a product. API gravity calculated how heavy (or light) an oil is compared to water. API Gravity is calculated according to the following equation:

$$API\ gravity\ (degrees) = \frac{141.5}{SG} - 131.5 \qquad (1)$$

Where SG is the specific gravity. Specific gravity is the ratio of the density of the oil product to a reference substance, in the case water at 60°F or 15.6°C). Note API gravity has no units, but is commonly referred to as being in degrees.

$$SG = \frac{\rho_{oil\ sample}}{\rho_{water}} \qquad (2)$$

Where ρ_{water} is assumed to have a density of 1000 kg/m^3. This relates to freshwater, sea water at 15.6°C will be more dense, its exact density will be a function of its salinity.

If we substitute ρ_{water} in to Equation 2 (we get SG = 1) and then substitute the resultant SG into Equation 1 we can see that the API gravity of water is 10°. This result means that oils that have a API Gravity greater than 10° are lighter than water, and thus will float on the water's surface. Whilst oils that have a API Gravity less than 10° are heavier than water and thus will sink.

Definitions the different oil types and the API gravity and Density are as follows:

Oil type	API gravity (°)	Density (Kg/m^3)
Light crude oil	>31.1	< 870
Medium crude oil	22.3 to 31.1	870 to 920
Heavy crude oikl	10 to 22.3	920 to 1000
Extra heavy crude oil	<10	>1000

Table Source: Wikipeadia: API gravity

As with most liquids the exactly density of an oil type is a function of its temperature. Thus when the temperature rises, oil expands and hence we see a reduction in its density. On the other hand when the temperature falls there is contraction and the density increases. The coefficient of thermal expansion is defined as:

$$\beta = -\left(\frac{1}{\rho}\right)\frac{d\rho}{dT} \qquad (K^{-1})$$

The density of the oil will influence the depth at which the oil will settle in water column i.e. the sea floor, the sea surface, or somewhere in between. It is important to remember that the density of the oil can change over time due to weathering, changes in its ambient temperature, the rate of emulsification etc.

In a cold water environment, such as those found under sea ice, the exact knowledge of the density (i.e. thermal expansion) of the oil is important, and therefore it is important to know the relationship between density and temperature

for the range of sea temperatures found under or near sea ice i.e. between -2° and + 10C.

3.2 Viscosity of oil

Viscosity is the resistance of a fluid to flow and shear. Generally speaking it is kinematic viscosity (resistance of the oil to flow and shear under the impact of gravitational force) that is a useful parameter. It is important to remember that viscosity (like density) changes with temperature i.e. a decrease in temperature produces and increase in the oil's viscosity. This change is not linear and that the changes are more pronounced at cold temperatures. For example in figure 11 we can see the relationship between viscosity and temperature for a particular oil type (ISO 68)

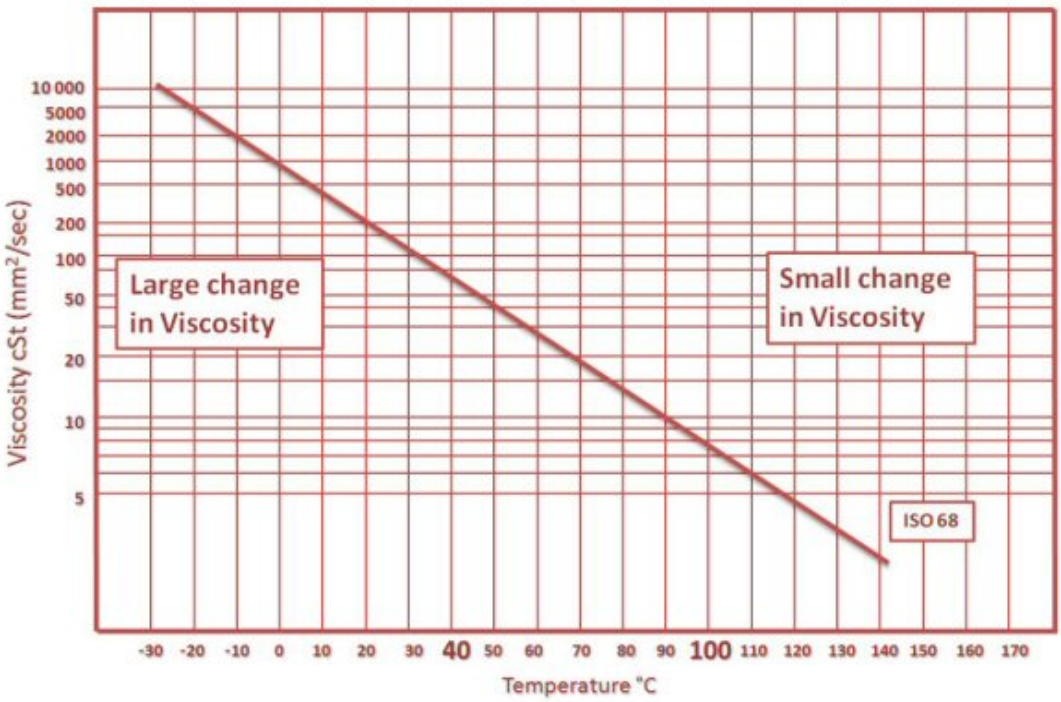

Figure 11 Change in viscosity of oil (ISO: 68) for a range of temperatures (ref: unknown)

From this figure we can clearly see that change in temperature has a dramatic impact on the viscosity of the oil, and that this change is not uniform. For example a rise in 10 degrees temperature from 0°C to +10°C is associated with a change of about 500 cSt (mm^2/s), whilst a change from 40°C to 50°C we see only a 50 cSt (mm^2/s). This difference becomes even more pronounced as the temperature

decreases. Interestingly water at 20°C has a viscosity of about 1 cSt or 1 mm^2/s, whilst ISO68 oil has a viscosity of around 200 cSt.

Furthermore the pour point is a key parameter that influences the spread of oil under or near sea ice. If the pour point within a few degrees of the water temperature the oil will be highly viscous oils and spread less quickly, but if the pour-point is lower than the ambient seawater temperature, the oil product will solidify shortly after contact with the ocean (Sebastião and Soares 1996). Furthermore.

3.3 Summary

Crude oil comes in a plethora of physical and chemical properties. Of these properties a full understanding of the density and viscosity of a particular oil product is needed if we are to model the behaviour of oil under sea ice. It is especially important to have this information over a range of realistic upper-ocean sea temperature regimes for the Arctic. This is because the temperature of the upper ocean fluctuates depending on the season, ice concentration, etc. (see ACCESS report D4.4.1). In the next section we look at the interaction of oil and different types of sea ice.

4. Sea ice and oil experiments

At present, it seems unlikely that governmental approval would be issued for full-scale evaluation tests involving oil spills in ice-covered seas. In fact *in situ* field studies are not ideal as they are subject to the environmental challenges, i.e. lack of control over environmental variables, and large logistical costs make it unrealistic to perform controlled experiments in the field. To avoid these limitations, controlled and repeatable experiments are ideal as they provide an opportunity to further our knowledge of the behaviour of oil under sea ice. These types of controlled experiments would be extremely difficult to perform under field conditions.

However access to large-scale facilities that have that have the ability to both grow sea ice and allow the spilling of oil are few and far between. Through access to additional funding schemes (both here in Europe and the US, see acknowledgments section) we were able to perform experiments at the US Army Cold Regions Research and Engineering Laboratory (CRREL), USA, and at Hamburg Ship Model Basin (HSVA), Germany.

Below we summarise the results from these experimental programmes.

4.1. CRREL: Experiments under a continuous sea ice sheet.

Our first set of under sea ice oil spill experiments were carried out at the US Army Cold Regions Research and Engineering Laboratory (CRREL) in Hanover, New Hampshire. Sea ice was grown to a thickness of 0.5 m in the outdoor Geophysical Research Facility tank (18.25 m long, 6.7 m wide, and 2 m deep) over the 2011-12 winter period leading up to experiments on January, 18-20, 2012. Hollows of dimensions of about 2.4 m by 1.2 m (in the along- and across-tank directions, respectively) were produced in the underside of the ice by placing insulating boards over the upper surface of the growing ice. Alaska North Slope (ANS) crude oil was injected into these pockets, where it pooled.

The properties of ANS are as follows:

Parameter	Value	Units
Density	0.858-0.887	kg/m3
API gravity	31.9°	° (degrees)
Total Sulphur	0.93	%m (as % of mass)
Viscosity at 30 °C	8.1	cSt
Pour point	-18	°C

Table. Characteristics of ANS (courtesy of BP)

A sensor suite including cameras, sonars, and a laser system was mounted on a trolley travelling on rails along the tank bottom. The trolley and sensor system was located beneath the hollows and oil was injected into the hollows from above the ice (Figure 12).

The oil released in the first injection remained in the hollow for the second release. Oil spread, detection and thickness measurements were conducted at a single location with the sensor platform 'parked' underneath the hollow. Observations of the spilt oil were also conducted by pulling the trolley along the tank bottom, passing under the oil-filled hollows.

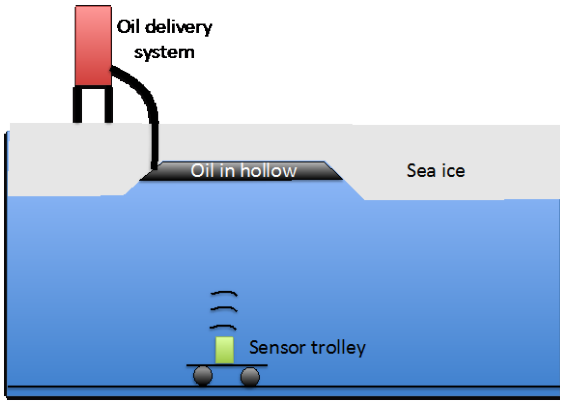

Figure 12a. Cartoon showing the experimental layout. The sensor trolley was located on tracks at the tank bottom. All sensors looked up towards the oil that was located just over a metre above.

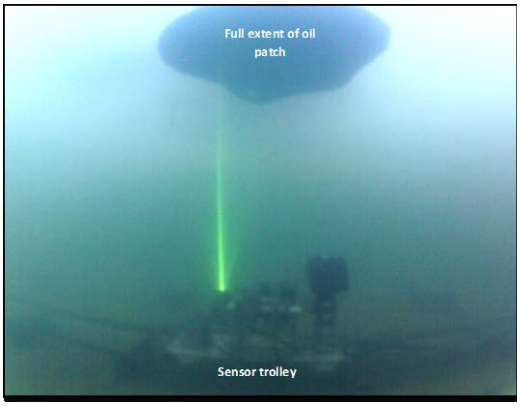

Figure 12b. Under sea ice oil slick and sensor trolley as viewed from the side using an underwater, wide angle "Go-Pro" camera. The green light is from a sheet laser that accompanied the sonar/cameras on the trolley.

The characteristics of the experiment are summarised in the following Table.

Characteristic	Value
Air temperature	-6.7 °C
Crude Oil Type	Alaska North Slope (ANS Crude)
Oil temperature	-4.2 °C
Times of oil injection	First: ~15:10 EST, Second: ~17:00 EST
Dimensions of hollow	2.4 m x 1.2 m
Depth of hollow (measured)	0.10 m

Characteristic	Value
Level ice thickness (measured)	0.5 m
Water temperature: (measured)	-1.3°C
Water Depth (approximate)	2 m
Sonar head distance to level ice (measured)	1.08 m
Sound Speed (inferred)	1430 m s^{-1}
Water salinity (inferred) **Water salinity (measured)**	25 psu 33 psu

Table. Parameters of the experiment conducted on 19 January 2012. Note the calculated water salinity of 25 psu was based on the measured water temperature of -1.3 (freezing point) and not the not the 33 psu as measured at the bottom of the tank. As the salinity (bottom) and water temperature (top) were measured at different depths this discrepancy could be due to haline stratification within the water column due to brine drainage.

4.1.1 Delivery of oil

The oil was delivered below the underside of the ice by way of a 20 litre pressurised canister-based system mounted on the surface of the ice. Crude oil was poured into the canister through an inlet at its top. When filled the canister was pressurised using an air compressor. A valve-tap at the bottom of the canister was opened and the highly viscous crude oil flowed within the oil-delivery hose, through a hole in the sea ice, to the underside of the ice (figure 13). This process ensured a stable delivery of oil to the ice underside and accurate determination of the volume of oil released.

The oil was released into the hollow through a PVC pipe frozen into the ice at the edge of hollow beyond the field of view of the sensors on the trolley. This ensured oil spread only within the hollow and did not flow back out of the hole and onto the ice.

Figure 13. Photograph showing the filling of the pressurised oil delivery system. This system allowed oil to be deployed efficiently and effectively as well as constraining the oil to the experimental hollow under the sea ice. No evidence of oil spreading beyond the hollow was seen.

4.1.2. Instrumentation

4.1.2.1 Camera system

Two upward-looking Prosilica high dynamic range cameras were mounted on the sensor trolley to provide overlapping views of the ice bottom. The camera systems are specifically built for extremely low-contrast applications that are typical of underwater (and under ice) applications. These are 12-bit dynamic range cameras (resolution of 1380 x 1024 pixels) that are individually calibrated and have a field of view (FOV) of 39.5 degrees horizontally and 30.5 degrees vertically.

With the cameras located at about 1.18 m from the underside of the sea ice hollow, the horizontal and vertical fields of view cover 0.5185 m^2 (0.85 m by 0.61 m) of ice bottom, and each pixel within the image represents a square of 0.06 cm by 0.06 cm (0.0036 cm^2). The cameras were set to take a photograph every 2 seconds. A continuous positive visual detection of the spreading patch can be used to yield information on the rate of spread, as well as providing visual confirmation of the presence or absence of oil.

4.1.2.2 Sonar Altimeter:

The 1.1 MHz echo sounder (Marine Electronics Ltd: Model 11001 Multi-Return Altimeter) has a 1.6° (+/-3dB) conical beam. When the instrumentation trolley was

located under the hollow the ice bottom was 1.18 m away from the sonar head, which insonified a footprint 3.3 cm in diameter (8.5 cm^2 in area) on the ice bottom. The sonar pulse length was 10 μs, corresponding to a length of 1.43 cm for a sound speed of 1430 m s^{-1}, and the return signal was sampled into bins of 1 μs duration (or equivalently 0.143 cm in range). The ping rate was set to yield an independent profile of acoustic return every 1 sec, however this rate drifted slightly and the results shown here have been shifted to the nearest whole second. This sonar was chosen because the high frequency (1.1 MHz) permitted excellent resolution, so that thin oil slicks might be detected.

The distance between the sonar head to ice bottom was physically measured (1.08 m), and from this measurement the sound-speed was inferred. Allowing for physical measurement error of ~1 cm for the distance between the sensor head to ice bottom, and for a 1 μSec error for the travel time recorded by the sonar, the sound speed was in the range 1417-1443 m s^{-1}. We have chosen a sound speed of 1430 m s^{-1} (see Table 1), which resulted in the sonar also showing that the separation between the sonar head and the ice bottom being 1.08 m.

The altimeter provided a time sequence of sonar returns, with a variability in range over time that can be related to reflection from interfaces between media of differing acoustic impedances. Changes in the strength of the return can be related to changes in these interfaces, although this can only been done qualitatively as it was not possible to calibrate the sonar.

4.1.3 Results

As soon as the oil was injected the oil flow along the underside of the hollow was clearly visible with both upward-looking high dynamic range camera systems (Figure 14). No additional illumination was needed to detect the oil, which is not surprising given the relatively thin ice (0.5m) and lack of snow cover. In regions of high snow loading on the sea ice (snow is very efficient at attenuating sunlight) or during the polar night additional light could also be provided by a strobe system, as is routinely used by camera systems on deep-sea underwater vehicles, although at the expense of increased power consumption. Further experiment with various lighting sources

are needed in order to determine the limits of what can be detected under differing scenarios, including cases in which oil is encapsulated by ice forming beneath it.

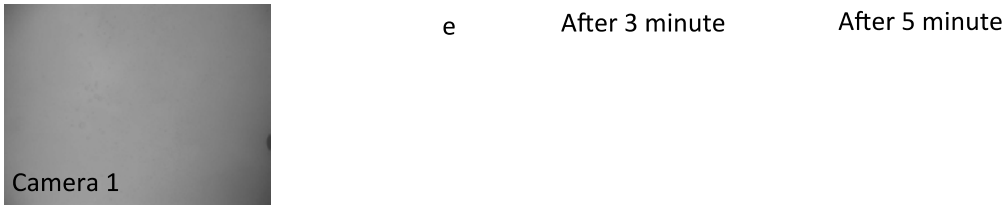

Figure 14. Selection of photos showing the flow of oil within the hollow over the first 5 minutes. The top time-series is from Camera 1 and the bottom series is from Camera 2. As the cameras were located at different positions on the trolley their field of view is slightly different. For example the oil entered the field of view of Camera 2 about 24 seconds before Camera 1. Field of view for each photograph is 0.5185m^2.

4.1.3.1 Spreading rate

A better understanding of the spreading rate of oil under different sea ice types is needed to accurately model the movement of oil under sea ice (Wilkinson et al., 2007). As the instrumentation trolley was stationary under the hollow for these tests, we can calculate the spreading rate of oil within the hollow from the time-lapse photography. A simple, automated, grey-scale thresholding method was used to discriminate between ice and oil in each photograph. This approach The area of oil was calculated based on the number of pixels (0.0036 cm^2) in the image that were classified as oil. The oil spreading rate was then obtained by calculating the change in oil area between consecutive images.

Our spreading-rate analysis spanned 5 minutes after the oil was first seen by the camera and involved the automatic segmentation of around 150 photographs. From Table 2 we can see that the oil spreading rate within the hollow gradually increased from just under 7 cm^2/s, before spreading out at a more constant rate (~9 cm^2/s).

For modelling purposes in-situ knowledge of the oil viscosity and pressure head will also be needed. We noted limitations to the experimental set up, namely the field of view from each camera did not encompass the entire oil slick and the slick was constrained by the hollow.

Time since oil was first seen by camera (seconds)	Mean oil spreading rate (cm^2/s)	Standard deviation spreading rate (cm^2/s)
60	6.56	2.99
120	8.32	2.99
180	9.25	3.15
240	9.79	3.13
300	9.41	3.23

Spreading rate of oil within the hollow, as calculated from a segmentation analysis of time-lapse photography.

4.2 HSVA: Experiments under a frazil, nilas and pancake ice.

In December 2013 oil under sea ice experiments were performed at the environmental test facility at Hamburgische Schiffbau-Versuchsanstalt GmbH (HSVA) in Hamburg, Germany.

The thought processes behind these experiments were that shipping and exploration for hydrocarbons in the Arctic is likely to occur during the summer open-water period. Consequently should an accident occur towards to end of this period, there is the possibility that oil could be distributed within a field of new ice. This new ice can take on three different characteristics. These are:

1. frazil,
2. nilas and/or
3. pancake ice.

The aim of our experiments was to grow these ice types and characterise the behaviour of oil under these ice types. To date very little information is available on the behaviour of oil spilled within the vicinity of these ice types.

4.2.1 Experimental set up

Experiments were run the Arctic environmental test basin at HSVA. This is a 30m

long, 6 m wide, and 1.5m deep basin in a climate controlled chamber. In order to provide the ability to perform experiments involving frazil, pancake and nilas the Arctic Environmental Test Basin at HSVA was sub-divided into three separate regions (see figure 15). This same tank set up has been used successfully for frazil, nilas and pancake experiments in the past (see Wilkinson et al., 2009).

Tank 1 was the quiescent tank and as such it was our aim to grow nilas in this tank. Tanks 2 and 3 had independent wave-makers installed and as such we aimed to grow frazil and then pancake ice in these tanks.

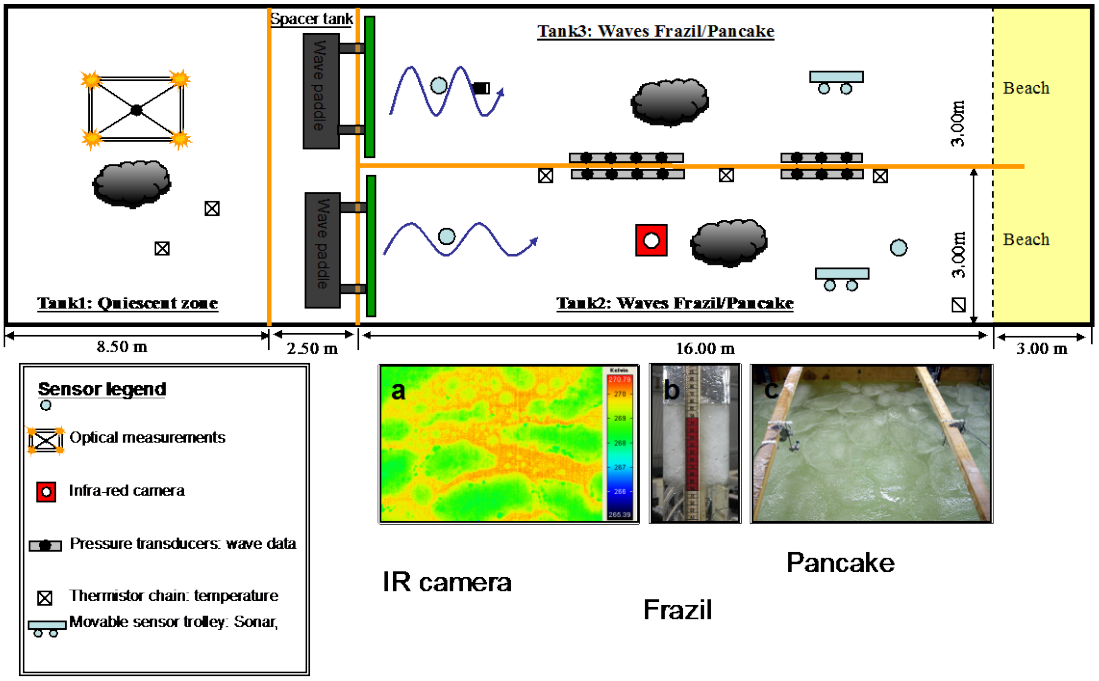

Figure 15 Layout diagram of the HSVA environmental test basin during our experiments in December 2013.

Unfortunately due to the heat exchange through the far wall and view port windows of the facility, significant ice formation was not achieved in tank 1, and thus the nilas experiments were performed in tank 2. At the bottom of each tank 'train tracks' allowed a 'train/trolley' to run along these tracks equipped with various sensors to be tested. The simultaneous mounting and recording of various sensors mounted on the trolley enables each sensor to be directly compared to each other as well as ensuring that each sensor's ability to detect oil is evaluated under the same environmental conditions. Tanks 2 and 3 were separated by a moderately stiff plywood divider.

For the spill experiments, “medium” crude was used, as this had properties similar to that of Alaskan North Slope crude (see table below). These include a density of 0.856-0.890 kg/m3, viscosity of 11.5 cSt (at 30 °C), and a pour point of -9 °C. The oil was deployed at temperatures of about 5 °C, so that melting of the ice by the oil was minimal. This also meant the oil was fairly viscous when spilled. A total of three oil spill experiments were carried out in tank 2 and 3.

	Alaska North Slope	**Medium Crude**	**Units**
Density	0.858-0.887	0.856-0.890	kg/m^3
Total Sulphur	0.93	1.4	%m
Viscosity at 30 °C	8.1	11.5	cSt
Pour point	-18	-9	°C

Table. Characteristics of the medium crude used within the HSVA experiments and the Alaska North Slope used during the experiments at CRREL.

4.2.2. Instrumentation

The following subsections describe the instrumentation deployed in the tanks.

4.2.2.1 Camera systems:

The camera systems in operation were a mixture of GoPros, a High-Definition underwater video camera, an IR camera, as well as a selection of hand-held digital cameras.

1) Three GoPro cameras were mounted overhead (looking down towards the tank) to image the ice and oil from above. These were placed at different locations along the whole length of the tank and took images at one minute intervals. These were generally in operation for the duration of the experiments.
2) Three GoPro cameras were mounted on the tank bottom looking upward toward the ice bottom. They also captured photographs at one minute intervals. Two of these cameras failed during the course of the experiment, but upward-looking imagery was obtained during most experiments.
3) An additional GoPro camera was mounted on the instrument trolley to provide

location information and imagery of each experiment

4) A high-definition underwater video camera was used to monitor each oil spill from below during the spill.
5) The infrared camera system was deployed on an overhead rail.
6) The participants used hand-held digital cameras to capture images of the experiments at different times and locations.

4.2.2.2 Sonar systems:

1) Two sets of Aquascat narrowband sonar transducers were deployed at different positions on the tank bottom. Transducers operated at nominal frequencies of 300 kHz, 500 kHz, 1 MHz, 2 MHz, and 5 MHz. One set of transducers was moved to the mobile instrument trolley during the spill experiments
2) Two sets of broadband transducers at frequencies of 350-565 kHz and 700-1050 kHz.
3) A Teledyne/Odom MB1 multibeam sonar system was deployed on the mobile trolley to provide sonar imagery of the ice underside of the ice and to explore the feasibly of estimating the angular dependence of the acoustic scattering.

4.2.2.3 Optical systems:

1) Three TRIOS hyperspectral radiometers were deployed to investigate the spectral attenuation and scattering of light through the oil spills. One irradiance and one radiance sensor were deployed on a mobile trolley, and one irradiance sensor was deployed above the ice to measure the incoming radiation field
2) The WHOI laser fluorometer was deployed on a separate mobile trolley and profiled the underside of the ice after the oil spills.

4.2.3 Oil Injection system

The oil injection system used at HSVA can be seen in figure 9. For each spill 10 litres (for frazil and nilas) or 5 litres (for pancake) of crude oil (at 5°C) was was poured into the funnel from pre-measured 5 litre cans. Care was taken that no air was introduced during this procedure. When the oil left the hose (diameter 5cm) it

separated into globules that rose up to the underside of the ice. The whole procedure took only a few minutes and the same technique was repeated at each of the three deployments.

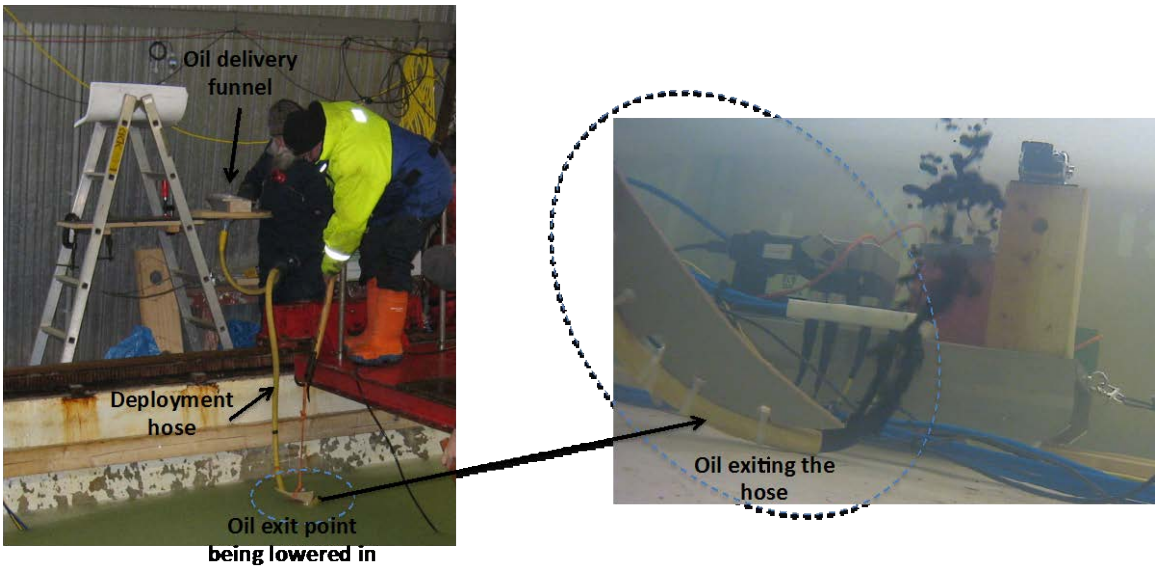

Figure 16 Oil deployment procedure at the HSVA experiments

4.2.4 Frazil Ice spill

On the 17th December a 10 litre spill of crude oil was performed under the frazil layer in in Tank 2. At this time the frazil layer was about a week old and the air temperature was below freezing. To produce the frazil ice we constantly ran the wave-maker at a frequency of 0.65 Hz. Before we spilled the oil the thickness of the frazil layer was measured as 8 cm (see adjacent figure). The frazil layer was a loose aggregation of independent frazil crystals, with no evidence of flocculation being present.

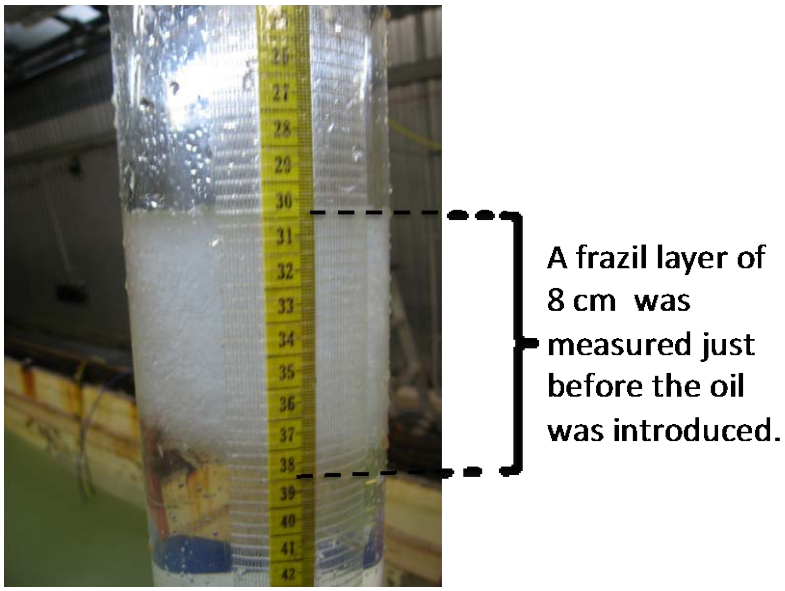

Oil was spilled below the frazil layer within a wave-field present (0.65 Hz). Due to buoyancy of the oil it floated up to the bottom of the frazil layer. Once at the bottom of the layer the oil did not spread laterally across the bottom of the ice, as with other ice types, but penetrated the frazil layer until it reached the uppermost frazil layer i.e. at the sea surface. Once the oil was at the surface it oil spread horizontally across the upper surface of the frazil/seawater (figure 17).

Figure 17. Oil pushed its way through the frazil layer and spread over the surface. Over time the size of the surface spill increased and its thickness decreased.

Once the spill had been completed the wave maker was turned off in Tank 2 and the surface began to solidify to form nilas (see experiment: Nilas). Once the frazil had frozen together to form a continuous sheet three ice cores were taken (see figure 18) (1) from near the centre of the spill, (2) from the edge of the spill and (3) in clean ice away from the spill. These cores were placed in a deep freezer (-20°C) for 24 hours. In order to determine how the oil had penetrated the frazil layer thick sections were made from these cores. Results from these cores also suggested that the oil was only located within the upper surface of the ice (see figure 19).

Figure 18. Results of the simulated spill in frazil ice. Most of the oil spread across the surface of the frazil. The blue boxes indicate where cores were taken and frozen for further analysis.

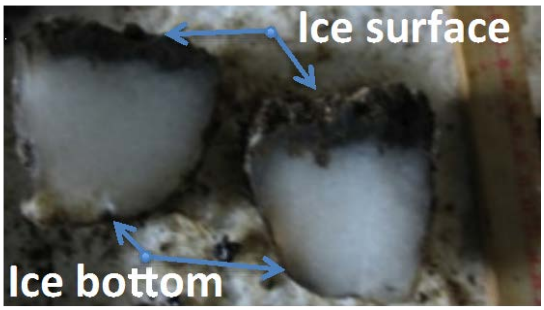

Figure 19. Example of Core 3 was taken from near the center of the spill. Oil was still fluid at this core site and as such oil coated the sample when it was removed. Upon cleaning only evidence of oil at the top of the ice was found.

This scenario was very unexpected and whilst we are still elucidating the exact mechanisms by which the oil was able to penetrate through an significant layer of frazil ice. We hypothesize that it due to the cyclic compression and relaxation mechanisms of passing waves. Field observations by Reimnitz and Kempema (1987) showed that the upper frazil layers are less agitated than the lower layers and thus it is this agitation of the frazil crystals that may allow the oil (as a buoyancy driven flow) to quickly penetrate through the frazil ice. Whether there is an upper limit on the thickness of the frazil that this process can occur is not known at this time. This very interesting result suggests that an oil spill occurring within an ocean dominated by frazil ice will most likely be confined to the surface layer of the sea ice.

4.2.5 Nilas Ice spill

Once the wave generator in Tank 2 was turned off the sub-zero air temperature enabled the frazil to begin to freeze from surface downwards. This produced an ice sheet of nilas. Given the thickness of the frazil layer (~8 cm) and that less than a day had elapsed only the first few centimetres of the ice were solid, with a loose aggregation of frazil crystals beneath.

On the 18th December (the day after the frazil experiment) a 10-litre spill of crude oil was performed under this nilas sheet. Even though the ice conditions were very similar to the frazil ice spill, the results were very different. Once the oil was released it spread into a roughly circular patch along the underside of the ice (figure 20 and 21). However it was clear from the images that the bottom topography was an irregular, undulating surface and this impacted the spread of oil. There was some visual evidence of oil migrating upwards through brine channels.

The results were very different to the previous oil in frazil ice experiment as the lack of wave energy inhibited the oil migration to the surface. The oil stayed at the bottom of the ice as can be seen in the figures above. However it looked like there was some migration toward the surface at discrete points, and it was this migration that produced the spotty nature to the image below.

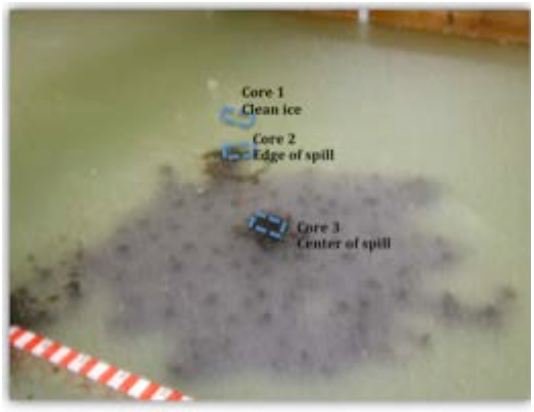

Figure 20. Image from above the ice. All of the oil was contained below the ice surface. Some migration toward the surface at discrete points caused the spotty nature to the image. The blue boxes indicate where cores were taken and frozen for further analysis.

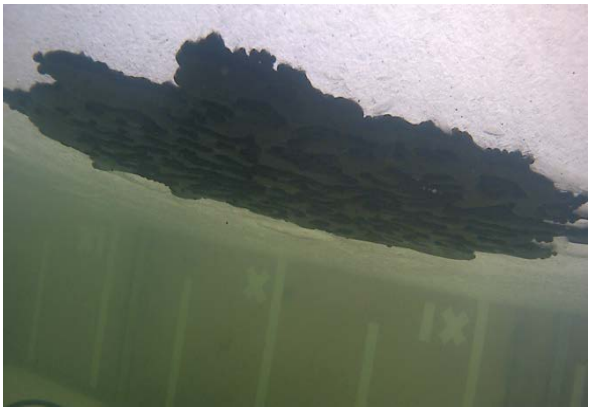

Figure 21. Image from below the ice. Aftermath of the spill in Nilas ice. All of the oil was contained below the ice surface. The bottom surface of the ice was an irregular, undulating surface. This under-ice structure influence the behaviour of the oil

At the frazil experiment three ice cores were taken (see figure 20) one from near the centre of the spill, another from the edge of the spill and a final core in clean ice away from the spill. These cores were placed in a deep freezer (-20°C) and thick sections were made from these cores. Results confirmed that the oil was contained at the bottom of the ice. However further sectioning of these cores provided evidence of the upward percolation of the oil through the porous ice (see figures 22 and 23).

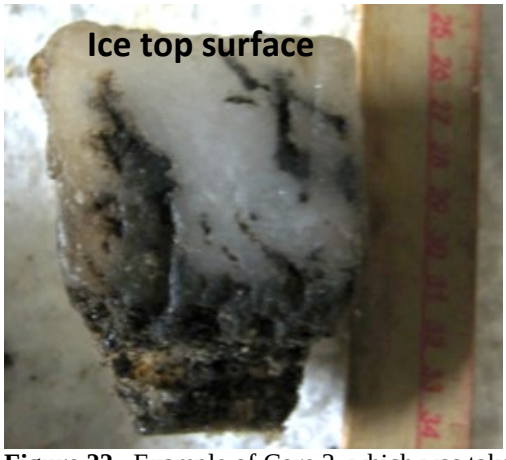

Figure 22. Example of Core 3, which was taken from near the centre of the spill. Oil was located at the bottom of the ice as well as in vertical channels within the ice.

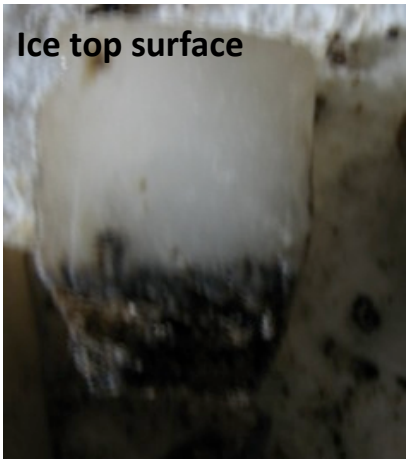

Figure 23. Further sampling of Core 3 indicate that the channels seen in the previous figure were not located throughout the ice lattice. This image shows oil located only at the bottom of the ice.

4.2.6. Pancake ice spill

Tank 3 was designated as the pancake ice tank. With the wave-maker continuously running for over a week the ice generated within this tank went though the process of forming frazil ice and then evolving in to pancake ice. At the time of the spill the pancakes were between 20 cm and 50 cm in diameter and around 10 cm thick.

In the late afternoon of the 18th December a 5-litre spill of crude oil was performed amongst the pancakes. The same technique was used to introduce the oil to the underside of the ice as with the other experiments. Once the oil left the hose the globules rapidly rose to the underside of the pancake. When the oil was in contact with a pancake it immediately flowed around the underside to gather in the open water region between individual pancakes (figure 24 and 25). Interestingly the oil did not seem to 'stick' to the underside of the pancakes at all.

Figure 24. Tank 3 showing the pancake ice before oil spill

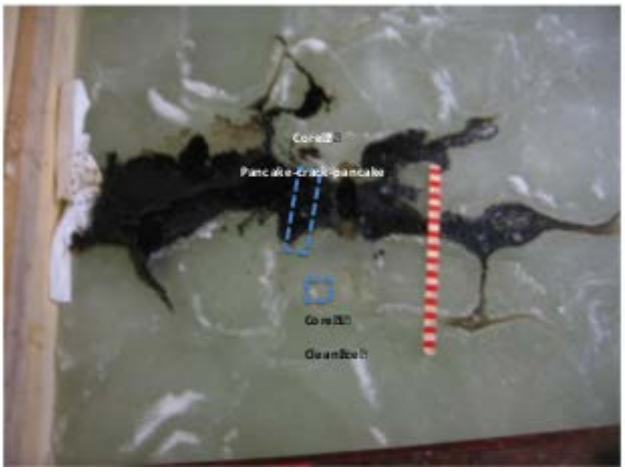

Figure 25. Tank 3 showing the pancake ice after the oil spill. The blue boxes indicate where cores were taken and frozen for further analysis

The cyclic motion of the pancakes, as the wave propagated through the pancake field, caused the open water region between pancakes to contract (at the wave trough) and then expand (at the wave peak). This concertina action had two influences on the behaviour and movement of the oil. These were:

1) The wave action accelerated the spread laterally around the pancakes.

2) The wave action enabled oil to be pumped over the rims of the pancakes. Once the over the rims the oil quickly spread over the surface of the pancakes.

As with the spread of oil within the frazil ice it seems that the incoming wave field plays a critical role in the spread of oil within a pancake field.

5. Surface roughness as a proxy for sea ice thickness from SAR

The ACCESS project “Resource Extraction” from work package 4.4.2 “Assessment of the behaviour of different types of oil and gas products in a cold water environment based on experiments and modeling” is a collaborative effort developed out of the need to assess the impact and consequences of economic activities related to oil and gas extraction in the Arctic, specifically oil spill responses in sea ice. An optimal way of doing a full assessment of oil 'holding' capacity within sea ice is to include under-ice topography parameters. This is particularly challenging as information on the under-ice topography is difficult to obtain. It would be much easier is we could obtain this information from satellite imagery. Is the surface expression of sea ice, as seen by remote sensing imagery, a proxy for under ice roughness? Thickness measurements from ground-truth data can coincide with the surface roughness from the backscatter of Synthetic Aperture Radar (SAR) from satellites. However, ground-truth data are difficult to obtain due to low temporal resolutions and spatial footprints of in situ data collections, moorings or ULS data. The importance of this study is that we can take advantage of a comprehensive high spatial resolution data set that covers a large area (LiDAR) to evaluate how well the wide swath Radarsat-2 ScanSAR Wide data estimates sea ice thickness.

This task evaluated the possibility of determining sea ice surface roughness from satellite measurements as several studies have indicated that it may be possible to use synthetic aperture radar (SAR) backscatter as a proxy for the underside roughness. In this task we determined statistical measures of the correlation between the roughness as derived from AUV multibeam sonar and the roughness from multi-polarisation SAR images.

5.1 Synthetic Aperture Radar (SAR) and Laser Altimetry (LiDAR) from the ICEBELL Campaign

The contribution from MET Norway for Task 4.4.2 compared Radarsat-2 SAR and LiDAR data records from November 28, 2010 which coincided with the ICEBELL Campaign. All SAR were made available by the Norwegian Ice Service (MET Norway) and Scottish Association for Marine Science (SAMS), and the LiDAR was provided by the British Antarctic Survey (BAS). This report describes the evaluation of Radarsat-2

capabilities to produce a more accurate sea ice proxy as a remotely sensed product for the ACCESS project which can be found at: (http://www.access-eu.org/). The aim of this report is to provide a preliminary statistical and comprehensive comparison of how we can infer sea ice thickness from Radarsat-2 and LIDAR images on Antarctic fast ice in the Bellinghausen Sea. A sea ice thickness proxy was developed by evaluating several different floes in one SAR image and corresponding scanning laser altimetry (LiDAR) sea ice freeboard measurements capturing the same floes. The three selected floes were a mixture of New Ice, First Year Ice (FYI), Rough First Year Ice (RFYI), and Second year Ice (SYI) in the the Bellinghausen Sea, Antarctica between Alexander Island and Latady Island (Figure 1) where we show the area swath coverage from both sensors. Though ideal conditions would have been selected on sea ice conditions in the Arctic, the best ground-truth measurements from the LiDAR were collected during the ICEBELL campaign in November 2010, which coincided with the aim of the ACCESS goals for this project . It is important to acknowledge that remotely sensed characteristics with floating ice in the Arctic and the Antarctic can differ greatly due to geophysical caveats in how the sensors detect surface roughness. Melt ponds on thick ice in the Arctic can be mistaken for open water when assessing surface roughness, whereas Antarctic thick FYI or SYI tends to have a flooded interface between the snow and sea ice due to a thick layer of snow pushing the ice downward (Weeks, 2010). Other processes such as brine flux, wind forcings, temperature, and heat flux through the ocean and sea ice interface affect growth and decay properties in sea ice, thus can greatly affect what is being remotely sensed. We can use information from SAR to infer sea ice thickness ranges based on sea ice types that may fall in a specific decibel (dB) range. However, this comparison with ground-truth data from the ICEBELL LiDAR allowed us to provide preliminary results over a larger area by analysing both datasets thickness and magnitude distribution to determine if there is any qualitative correlation.

5.2 Data Description

5.2.1 Bellinghausen Sea

Coincident laser altimetry (LiDAR) and Synthetic Aperature Radar (SAR) data were collected during the ICEBELL campaign in the Bellinghausen Sea between Alexander Island and Latady Island in November 2010 (Figure 1). This area was deemed to be acceptable for comparing surface roughness to obtain sea ice thickness from SAR because the sea ice floes corresponding to the LiDAR were mainly first-year sea ice types in various stages according to observations collected. Antarctic sea ice has a mean of approximately 1.0 – 1.5m and does not retain as much second year ice as the Arctic (Sandven and Johannessen, 2006). Therefore, the outcome of the preliminary results in this report can be representative of Arctic sea ice interpretations of sea ice thickness.

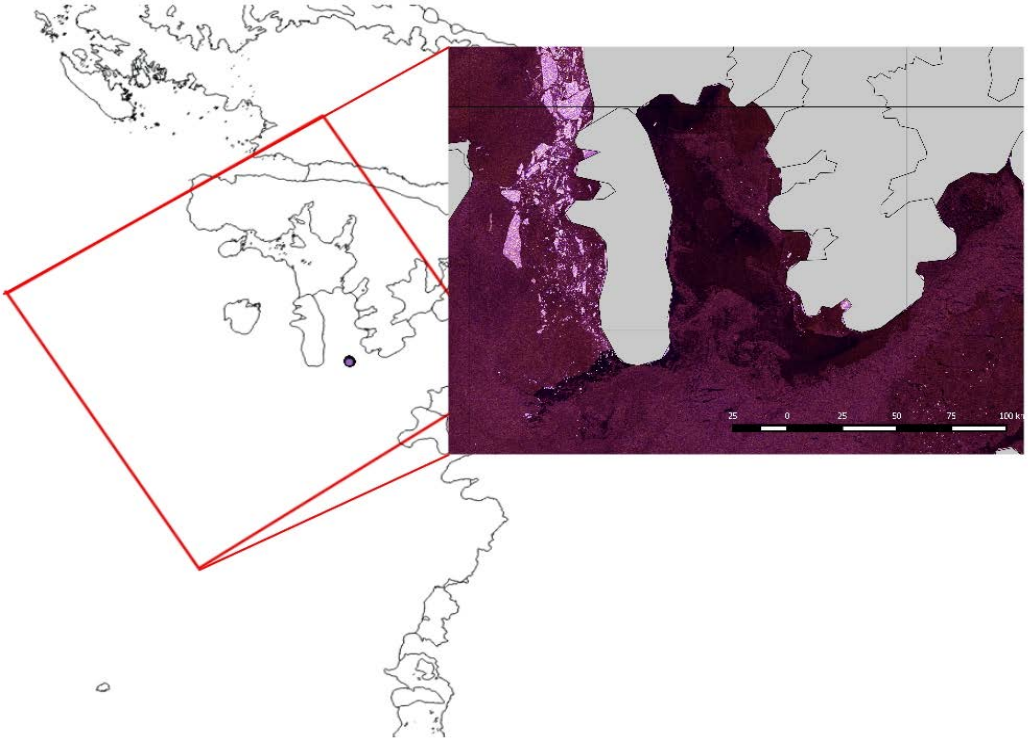

Figure 26. Location of data collected from ICEBELL campaign on floe 1-3 in the Bellingshausen Sea, Antarctica.

Upon visual observation, the three floes selected include a mixture of FYI and smaller floes of thick FYI/SYI, and thin ice types. The largest floe, Floe 1, shows the largest variety of these ice types next to Floe 2 which shows a more homogenous flow. Floe 3 appears to contain some new ice and smaller thicker ice floes. The floe

areas range between 0.1 km2 to 3.2 km2 , thus may be susceptible to pixel mixing and will give a less accurate thickness distribution when compared to SAR data.

5.2.2 Radarsat – 2 Synthetic Aperture Radar

Radarsat-2 is an Earth observation satellite provided by the Canadian Space Agency that includes a Synthetic Aperture Radar (SAR) active microwave sensor operating in the C-band (5.405 GHz) . Currently, this is one of the preferred sources for sea ice monitoring and mapping because it contains multiple polarization (HH, HV, VV, VH) modes which are useful for separating sea ice from open water. Additionally, multiple polarizations can be used to provide thresholds for sea ice surface roughness which can directly correlate to sea ice thickness (Moen et al 2013). The Radarsat-2 dual polarization ScanSAR Wide swath (HH and HV) was used which covered a 500 x 500 km area with a ~50 - 100 m spatial resolution and an incidence angle between 20°- 49°. The ScanSAR Wide mode (SCW) data were processed as a ground range and multi-looked processed as a Georeferenced Fine (SGF) image (also known as a Path Image). The pixels in SAR images are unitless measurements of backscatter coefficients (sigma nought, σo) on a decibel (dB) scale which gauges the level of roughness being returned from the surface.

A comprehensive background on sea ice properties can be found at Casey, 1992 and Weeks 2010 and will not be discussed in detail in order to provide a concise analysis of sea ice thickness outcomes from SAR data for this report. Many sea ice features have unique microwave signatures that have been documented with the use of radar (Casey, 1992, Drinkwater et al., 1995 and Morris et al., 1996). Additionally, Antarctic sea ice has a lower mean backscattering coefficient than that of the Arctic attributed to younger sea ice and higher salinity levels. Previous assessments of Antarctic sea ice in the Weddell Sea and Bellingshausen Sea have similar backscatter signatures with FYI and SYI and have been measured between approximately -17 dB and -9 dB for all ice types, depending on surface roughness, which were used as the parameters for this study (Drinkwater et al., 1995, Morris et al., 1996, and Tekali et al., 2009). Backscatter values increase with higher surface roughness (vs. smooth) and decrease with increasing incidence angles (vs. low angles). The continued sea ice melting into the summer season also causes backscatter values to become lower

but could be attributed to increased snow melt. (Haas, 2001 and Wilmes et al, 2009). Due to seasonal influences of radar signal strength RFYI can be difficult to separate from SYI at low incidence angles, during the melt season (spring) and the differences are reversed depending on how much snow cover is present (Drinkwater et al., 1995, Wilmes et al. 2009 and Weeks, 2010). Haas, 2001 measured a range for sea ice dB values in the Winter to be -15.0±0.8 and -8.5±0.8 in the Summer. Since the backscatter is a function of incident angle and polarization, it is important to note the range of dB values established from Drinkwater et al., 1995, Morris, et al. 1996, and Haas, 2001 were based on slightly different frequencies than Radarsat-2, but the correlation with incident angle is still relevant to this study. The mean sea ice dB values for rough FYI, smooth FYI, and mixed SYI are -14dB, -9dB, and -13dB respectively. On average, pancake ice will have a backscatter > -20 dB at incidence angles < 50o and first-year ice between -10 to -35. This range can be between -10 and -40 based on the amount of ridging and roughness on the surface. Medium thick FYI show little differences at incidence angles > 45o, but can be up to -10dB difference between thick FYI and SYI depending on the surface roughness (Drinkwater et al. 1995). All floes were measured at incidence angles between 31o and 32o which allows us to compare these dB values against baseline date previously measured in the same region and the Weddell Sea (Drinkwater et al, 1994, Drinkwater et al, 1995, Morris et al., 1996, Haas, 2001, and Tekeli et al., 2009).

HH and VV are co-polarised channels where the receive polarisation is the same as the transmitting signal. The HV and VH channels are the cross-polarisation channels where the receive polarisation is different to the transmitting signal. The polarization is a significant influence on backscatter signatures because vertical channels appear darker than the horizontal channels. The HH channel picks up on surface roughness more which equals to a higher backscatter and the VV channel is more susceptible to signal absorption. This leads to different interpretations of the ice surface because the HH channels have a difficult time to distinguish between thin ice and thick ice floes due to the surface roughness. The VV separates floes easier but mixes thin ice with open water and may also be more sensitive to surface flooding. FYI is normally

bright at the HH and VV channels but new ice and melting ice will exhibit lower dB values. Unfortunately, it is not possible to have both co-polarized channels (HH and VV) in a single Radarsat-2 dual polarization image unless one of the quad-polarization imaging modes, with much more limited spatial coverage, is used. The HV channel is a good combination because it separates floes from open water with the vertical, as well as picks up on the ridging features due to the horizontal polarization.

5.2.3 Laser Altimetry

A Light Detection And Ranging system known as LiDAR has been used to examine sea ice with the onset of ICESat (The Cloud and Land Elevation Satellite) in 2003 (Weeks, 2010). Lidar is a laser altimetry device that emits light to the surface and measures the return. LiDAR can be used to measure sea ice thickness and snow depth by detecting freeboard; therefore, it is essential to know the elevation and deviation from the mean surface and sea ice density (Kwok and Cunningham, 2008). This is a useful device to collect ground truth because it provides a high spatial resolution (in centimeters) and is able to cover large areas to coincide with remotely sensed data. The LiDAR used for the ICEBELL campaign was a Riegl q140/240 scanning lidar which was used in conjunction with a Honeywell GPS/INS and multiple GPS recceivers (Javad, Trimble, Ashtech). It was connected to the BAS MASIN twin otter aircraft: (http://www.antarctica.ac.uk/living_and_working/aircraft_and_vehicles/aircraft/twin_otter.php).

5.3 Methods

Due to the temporal difference of the Lidar and SAR data as stated above, a qualitative comparison was evaluated for sea ice thickness distribution in three floes. They were selected based on visual analysis by overlaying the LiDAR on the SAR and selecting the most distinct floes. Due to ocean and wind forcings, the drift of sea ice makes it difficult to schedule the SAR acquisition at the exact same time as the LiDAR collection. By trying to compare both datasets on a one-to-one basis may

introduce more error for those stated reasons. Therefore, the floe tracking method for this study is sufficient for our purposes.

5.3.1. LiDAR Preprocessing

A Terrain 360 deg scanning LIDAR collected surface measurements over floes that contained a mixture of broken up New Ice, FYI, and SYI. Additionally, the floes appear to be located near an eddy which may influence their thickness distribution. The angle of the beam to the surface was between 70º– 132º. The total preprocessing of the 3D characterization of freeboard and snow depth LiDAR data was processed by the British Antarctic Survey (BAS). The LiDAR was corrected for

sea ice drift and the large number of tracks collected during the ICEBELL were mosaicked for ease in working with the comprehensive data set for an area. The freeboard measurements represent a combined snow and ice freeboard thickness.

Initially the lidar positions were matched up to SATICE buoys by isolating the data and time range for the LiDAR and overlaying it against the research ship which was moored up to the floe. The SATICE times were interpolated to SATICE positions to ~1 – 2m of the LiDAR measurement postions. The distance of the SATICE points were checked to confirm it's proximity to the LiDAR area and were used as reference positions to match sea ice drift and rotation correction. The mosaics were created by matching individual lidar tracks together based on sea ice elevations in the overlaps.

The first track over sea ice in the data was used as a reference track, and its position was unchanged. There can be many tens of minutes between that first track and the track that overflies the SATICE instrument. In that time there could be a noticeable rotation in the floe positions, which will be missing in the mosaic as it is matched to the state of rotation/alignment of that very first track. The

difference between the SATICE angles and the buoy angle and LiDAR mosaic angles corrected the mosaic alignment. Quantum GIS was used to segregate discernable floes in the LiDAR ASCII data. These were initally overalyed onto SAR imagery to clarify they are clearly defined in the raster data as well. The three floes were separated from the mosaicked LiDAR data by manual digitization and converted into vector files for further information extraction (Figure 2).

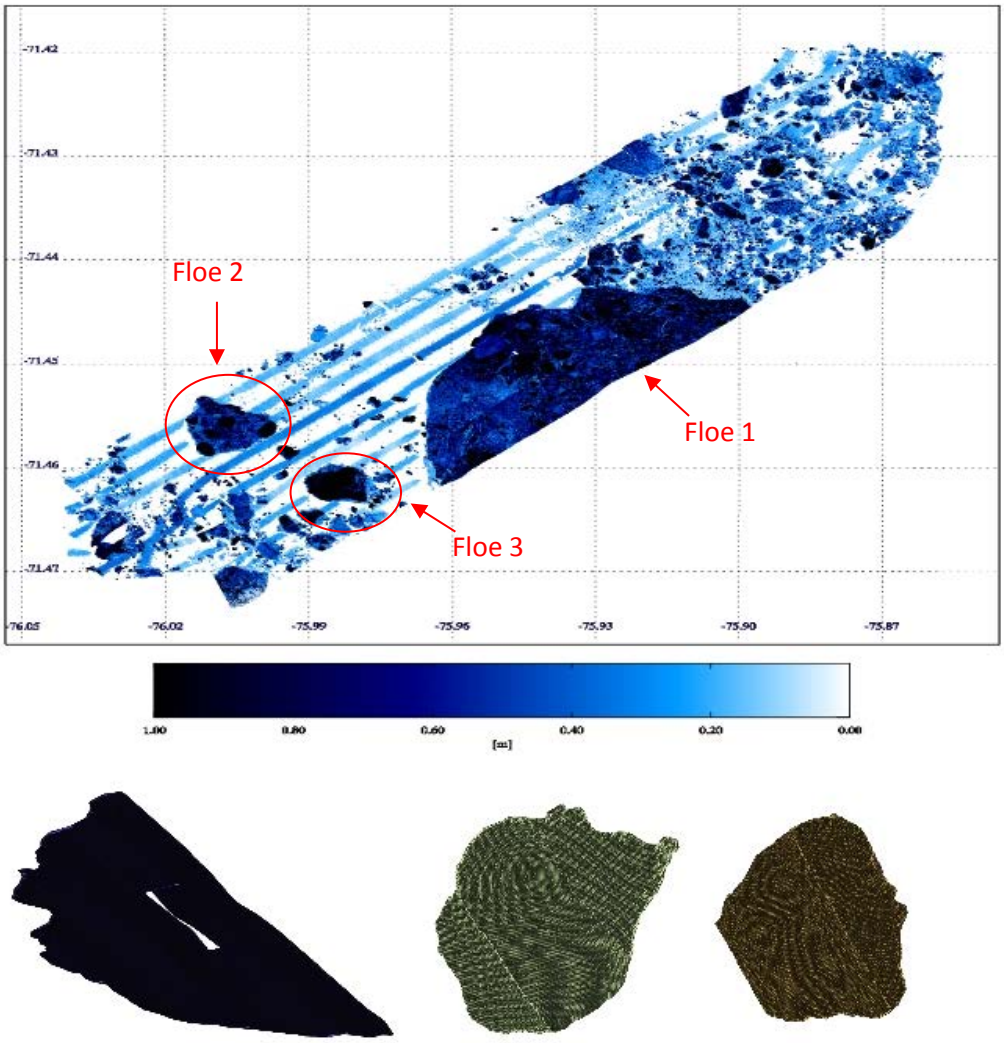

Figure 27. Floe 1(left), floe 2 (middle), and floe 3(right) vector files and locations on LiDAR mosaic.

The sea ice freeboard was extracted from the attribute tables and converted into a probability density function in order to get a general distribution for each floe.

5.3.2. Radarsat -2 Preprocessing

The preprocessing for the Radarsat-2 data required an initial remapping to Polar Stereographic/WGS84 to match up the latitude and longitude coordinates from the LiDAR, subsequently followed by converting the linear to dB coordinates. The following conversion was used for to calculate the dB:

$$dB = 10 * Log_{10}\,(Intensity)$$

The dB ranges fell between -5 and -20 which is appropriate from previous studies of sea ice in this area (Haas, 2001 and Tekeli et al., 2009).

5.3.3. Masking Region of Interest (ROI) for SAR

The three floes were subset from the SAR image by specifying a Region of Interest (ROI) with vector masks. Shapefiles were created as placeholders and masks were manually digitized to capture the correct floe area (Figure 3).

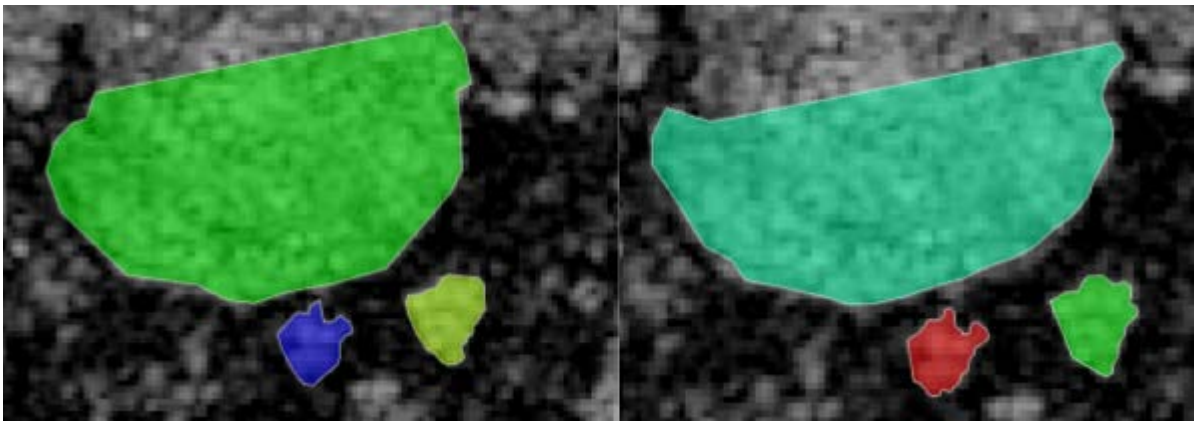

Figure 28. ROI 1(left) and ROI 2(right) showing slight differences in the manual creation of ROI for Floe 1, Floe 2, and Floe 3.

Though it is important to try to match the SAR and LiDAR floes exactly, the differing spatial and temporal resolution will not allow direct correlations. Additionally, the coarse nature of probability density functions allow the omission of some values, without affecting the overall distribution. Therefore, two different ROI's were created for the same SAR image and fit to one another to determine if the differences are significant. Both ROI areas capture the correct floes but are drawn differently to include or exclude additional pixels and then correlated. Figure 4 shows a good

correlation and that the differing amount of pixels and manual creation of ROI's do not significantly affect the regional distribution of dB values.

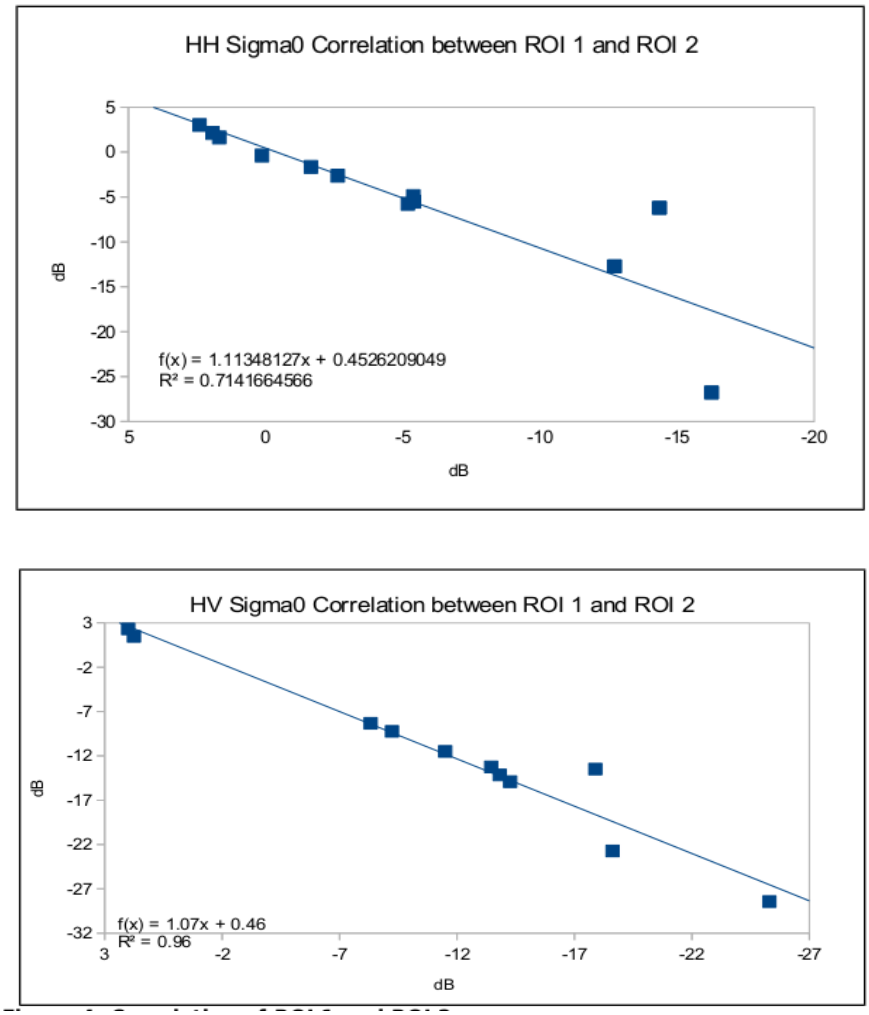

Figure 29. Correlation of ROI 1 and ROI 2

As previously mentioned, the HH channel is considered to work well in picking up smooth new ice and open water and the HV channel is good at picking up ridging and deformation features. From this average backscatter values are higher with the HH band than that of the HV (Figure 5). Therefore the HH and HV channels were used together to optimize a more accurate analysis for ice conditions (Arkett, et al. 2003).

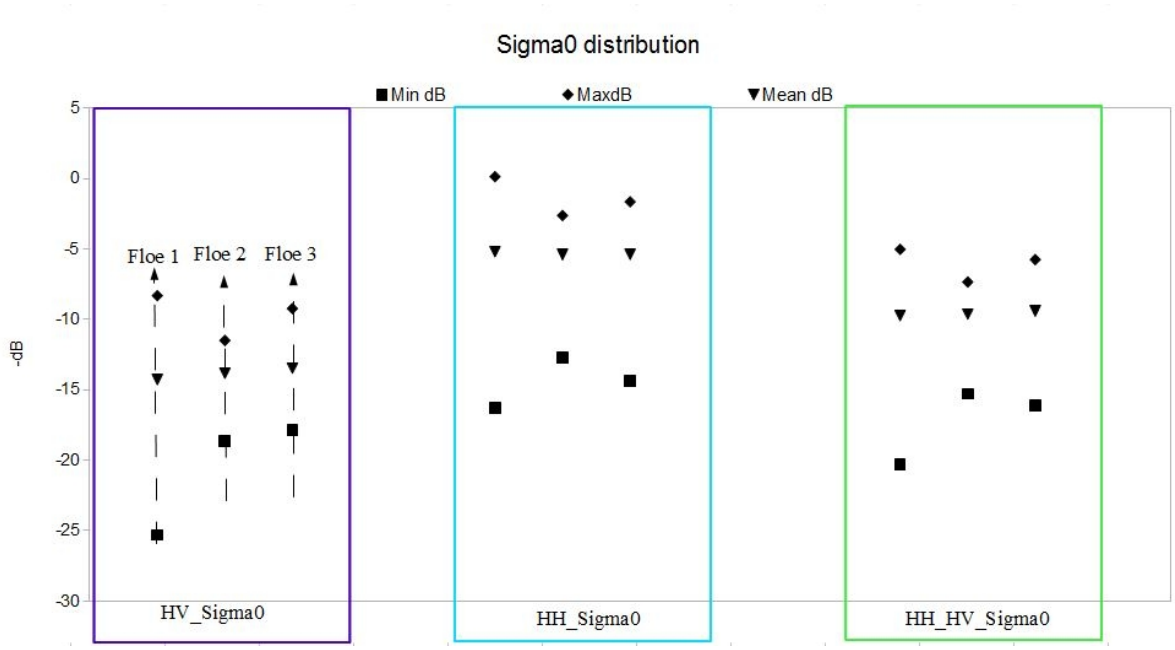

Figure 30. Comparison of minimum, maximum, and mean values for HH, HV, and HH/HV polarizations.

5.4 Results

Probability density functions (PDF) for the SAR and LiDAR are shown in figure 6 and 7 for the three floes. These distributions are based on these two datasets and the following analysis will not include information on mean air temperatures, wind conditions, or snow cover. The distribution of ice types from the LiDAR for floe 1 and floe 3 show a good correlation in both the SAR and LiDAR. The LiDAR swath image in figure 2 displays a clear mixture of the broken up FYI, some smaller thicker FYI or SYI, and new ice in between the smaller floes, and floe 2 appears to be a uniform floe of either rough FYI, or SYI. The highest PDF for floe 2 from the LiDAR is 1.2m

which suggests it is between thick FYI according to the World Meteorological Organziation (WMO) sea ice symbology. Thicknesses between 0.4m and 0.7m dominated floes 1 and 3 and show similar amounts of thickness distributions except floe 1 has a larger amount of ice types at 0.8m. However, floe 3 consists of more thick FYI ice types. Based on sea ice thickness estimates floe 1 and 3 contain approximately 80% of FYI and floe 2 at 60%.

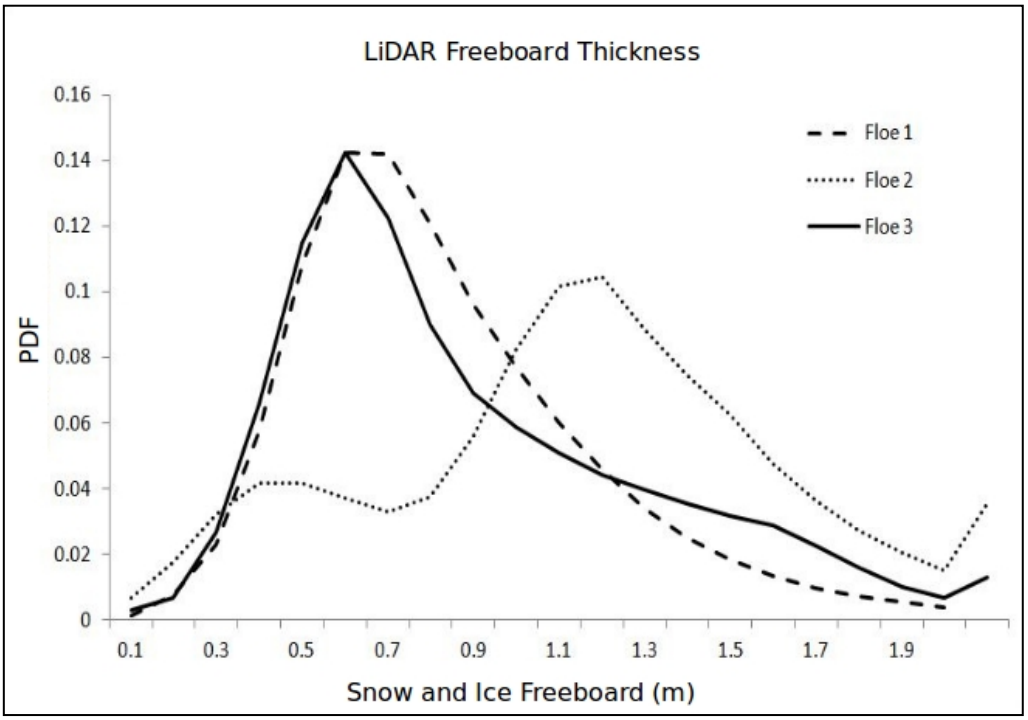

Figure 31. LiDAR sea ice freeboard distribution for floe 1-3.

Surface roughness causes higher dB due to the nature of scattering mechanisms. Backscatter values on both FYI and SYI ice types are similar and not easily distinguishable which is shown in all three floes. The upper end of backscatter ranges fell between -7 and -8 for all floes due to this reason. These are average ranges expected from Drinkwater et al., 1994, Drinkwater et al. 1995, Partington and Hanna, 1994 , and Morris et al. 1996. From fig 6 we see that Floe1 and 3 look similar in freeboard whilst Floes 2 has a larger freeboard (although there is a bimodal distribution to the result). Floe 1 and 3 show a better correlation in dB values similar to LiDAR measurements in figure 6, whereas floe 2 clearly reflects more of a homogeneous sea ice type between -7dB and -13dB, except for one peak at -11dB. This suggests one area of flat smooth FYI or new ice. Floe 2 and 3 peak at -8, whereas floe 1 shows the highest frequency at -9 and one at -11 which may be attributed to a small area of smoother ice that hasn't deformed yet, or the beginning stages of flooding between the snow and sea ice. Floe 1 displays a smother curve implying it consists of several different sea ice types and roughness postulated from the LiDAR image. The small rounded floes with smaller floes of thicker ice may have developed from broken up FYI floes but the relatively high backscatter values from

all the flows may be linked to surface roughness, brine wicking from seawater flooding between the snow and ice (Lytle et al, 1996), or ice formation in the snow layers, which influence high scattering (Morris et al., 1996). Lower backscatter values <-10dB are probably related to younger undeformed FYI or flooding from snow melt (not seawater) which make up approximately 35-40% of all floes. Additionally, November in the Antarctic is a transitional period into the Austral Summer, therefore, the rising ice-surface temperatures could be influencing the HV as high salinity in young smooth ice can also cause lower values in backscatter signatures (Drinkwater et al, 1995).

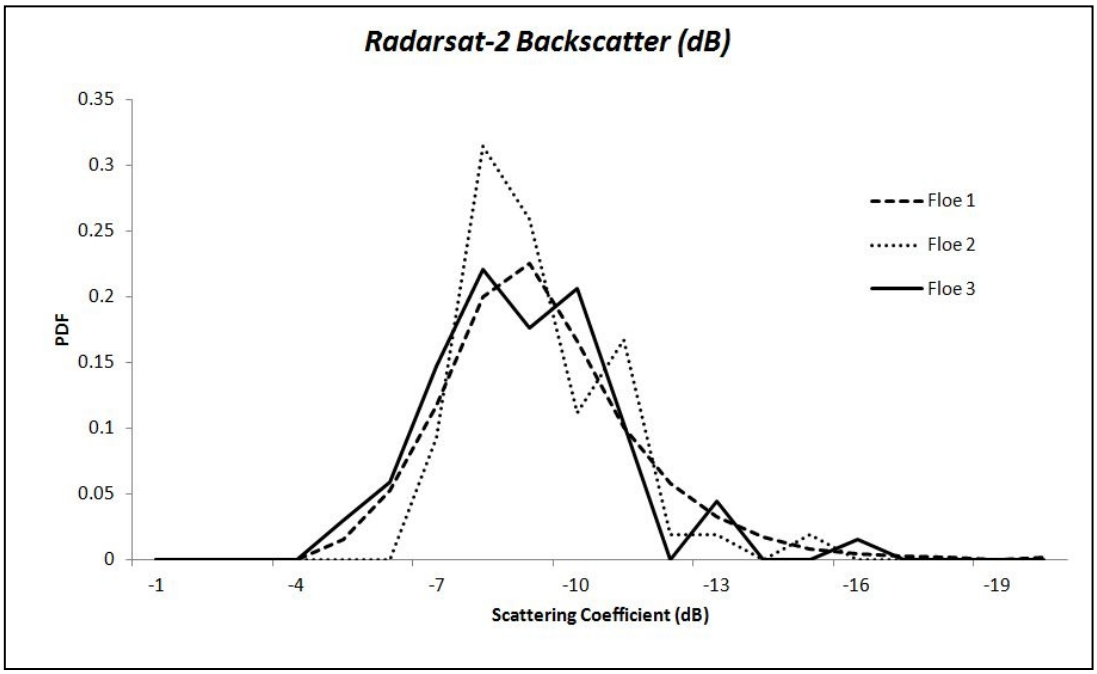

Figure 32. SAR dB distribution for floe 1-3

5.5 Conclusions

Initial results suggests that there may be a correlation between LiDAR freeboard distribution and Radar backscatter. However we are at an early stage and without knowledge of meteorological conditions combined with sea ice and snow properties (i.e. salinity, snow thickness, brine wicking, slush formations, heat flux as the transference of net radiative and sensible heat flux, and air temperatures),it is difficult to provide a comprehensive comparison with the SAR and LiDAR based on 3 floes in the same area. Additionally, the floe areas chosen may be too small and thus do not represent sea a full sea ice thickness distribution of the area. Though it may

be difficult provide an accurate correlation in this study, we can establish a range in which further comparisons of both datasets can be compared. Further research is needed and the ICEBELL campaign collected several tracks of extremely useful LiDAR data in the Bellingshausen and Weddell Seas which have been mosaicked by the British Antarctic Survey that coincide with 7 different areas where we have more satellite data (TerraSARX, PolSAR, Radarsat-2, ASAR) provided by Met.Norway and SAMS. We plan to take the full LiDAR dataset and compare it to all relevant satellite images for a full quantitative comparison to determine how well we can assess sea ice thickness from SAR backscatter. We will also include in situ measurements collected during the cruise in order to provide a robust analysis for this study. Satellite derived ice roughness would provide a realistic means of providing almost synoptic wide area coverage of ice covered areas for both detecting and assessing the flow and coverage of an oil spill. Future plans include using these ranges and dB values from the Antarctic and extrapolate the values for sea ice thickness for the Arctic which could provide a better understanding of how sea ice thickness may be detected from SAR in the case of an oil spill.

6. Summary

Our combined results should ensure that we are better able to understand the temporal and spatial evolution of oil dispersal under different types of sea ice. This delivers a huge leap beyond the state of the art understanding of oil behaviour under sea ice. These results can now be applied to the modelling work of Task 4.4.3.

7. Acknowledgements

This work could not have been performed without the outside help of a number of organisations and people. Additional support for these tests was obtained from Alaska Clean Seas, and the Oil Spill Recovery Institute. The "Oil under Ice" tests at HSVA were supported by the European Community's 7th Framework Programme through the grant to the budget of the Integrated Infrastructure Initiative HYDRALAB-IV, Contract no. 261520. We would also like to thank BP for their help in obtaining the crude oil for the HSVA experiments. Teledyne Odom graciously loaned the MB1 sonar. The Center for Coastal and Ocean Mapping at the University of New Hampshire provided substantial assistance with calibration of the sonar and with shipping .

Furthermore numerous people and institutes (outside ACCESS) were involved in these experiments including:

- CRREL: L. Zabilansky
- CU: D Chayes
- OSRI: S. Pegau
- URI: C Roman
- WHOI: T Maksym, H Singh and C Basset

We would also like to express our gratitude to Vicky Hamilton-Morris and Russ Ladkin at BAS for their help with the LIDAR data, A big thanks goes to the Ice-Bell team who collected these data.

References

Arkett, M., Flett, D., and De Abreu, R. (2003). C-Band Polarization SAR for Ice Monitoring – What Can It Do for the Canadian Ice Service. ESA Earthnet Online

Barnes, P.W., E. Reimnitz, L. Toimil, and H. Hill. (1979). Fast Ice Thickness and Snow Depth in Relation to Oil Entrapment Potential, Prudhoe Bay Alaska. USGS Open File Report 79-539, Menlo Park, CA.

Bonn Agreement (2004) http://www.bonnagreement.org/eng/html/welcome.html

Daly, S.F. & Colbeck, S.C., 1986. Frazil ice measurements in CRREL's flume facility. *8th International Symposium on Ice*. University of Iowa, Institute of Hydraulic Research Location: Iowa City, pp:427-438.

Dickins, D., J. Overall and R. Brown (1975), *Beaufort Sea Project Tech. Rept. 27*, Inst. Of Ocean Sciences, Victoria B.C.

Drinkwater, M., Early, D. and Long, D. (1994), ERS-1 Investigations of Southern Ocean Sea Ice Geophysics Using Combined Scatterometer and SAR Images. Geoscience and Remote Sensing Symposium, 1994. IGARSS '94. Surface and Atmospheric Remote Sensing: Technologies, Data Analysis and Interpretation., International (Volume:1).

Drinkwater, M., Hosseinmostafa, R., and Gogineni, P. (1995). C-band Backscatter Measurements of Winter Sea Ice in the Weddell Sea, Antarctica. International Journal of Remote Sensing. Vol. 16, Number 17, 20.

Greene, G.D, Leinonen, P.J and Mackay, D. (1977). An Exploratory Study of the Behaviour of Crude Oil Spills Under Ice. *Canadian Journal of Chemical Engineering* 55, 696-700.

Haas, C. (2001). The seasonal cycle of ERS scatterometer signatures over perennial Antarctic sea ice and associated surface ice properties and processes. Annals of Glaciology, Vol 33 33:69-73.

Keevil, B.E. and R. Ramseier (1975), In: *Proceedings of the 1975 Conference on Prevention and Control of Oil Pollution.* American Petroleum Institute, USA. pp 497-501.

Kovacs A., R. M. Morey, D. F. Cundy, G. Decoff. (1981). Pooling of oil under sea ice. In Proceedings POAC 81: Sixth International Conference on Port and Ocean Engineering under Arctic Conditions, Quebec, pp. 912–922.

Kovacs, A. (1977). Sea Ice Thickness Profiling and Under-Ice Oil Entrapment, Paper OTC2949, Proceedings 9th Annual Offshore Technology Conference, Houston.

Kwok and Cunningham, (2008). ICESat over Arctic sea ice: Estimation of snow depth and ice thickness. Journal of Geophysical Research. Vol. 113, C08010, doi:10.1029/2008JC004753.

Leonard, G., Shen, H.H., and Ackley, S.F., 1999. Initiation and Evolution of Pancake Ice in a Wave Field, *Antarctic Journal*, 32:53-55.

Lytle, V.I., Jezek, K., Gogineni, S. and Hosseinmostafa A. (1996). Field observations of microwave backscatter from Weddell Sea, Int. J. Remote Sensing, 17, 167-180, 1996.

Moen, M. A., Doulgeris, A. P., Anfinsen, S. N., Renner, A. H. H., Hughes, N., Gerland, S., & Eltoft, T. (2013). Comparison of automatic segmentation of full polarimetric SAR sea ice images with manually drawn ice charts. The Cryosphere Discussions, 7(3), 2595-2634.

Morris, K., Jeffries, M., and Li, Shunsun. (1996). Sea Ice Characteristics and Backscatter Variability in the Bellinghausen Sea, Antarctica. Proceedings from the Fourth Symposium on Remote Sensing of the Polar Environments, Lyngby, Denmark. ESA SP-391.

Partington, K and Hanna, M. (1994). Modelling radar sea ice backscater in support of the ERS-1 SAR. EARSeL Advances in Remote Sensing Vol. 3, No. 2 - XII.

Reimnitz, Erk & Kempema, E.W., (1987). Field observations of slush ice generated during freeze-up in Arctic coastal waters *Marine Geology* 77 :219-231.

Sandven, S., Johannessen, O., and Kloster, K. Sea Ice Monitoring by Remote Sensing.(2006). Encyclopedia of Analytical Chemistry.

Sebastiao P, and Soares CG. (1995). Modeling the Fate of Oil Spills at Sea. Spill Sci Techn Bull 1995

Scoresby, W., (1815): On the Greenland or Polar ice. *Memoirs of the Wernerian Soc*. 2 261-338 (repr. 1980, Caedmon, Whitby)

Tekeli, A., Kern, S., Ackley, S., Ozsoy-Cicek, B., and Xie, H. (2009). Summer Antarctic sea ice as seen by ASAR and AMSR-E and observed during two IPY field cruises: A case study. Annals of Glaciology 52(27), 57A091.

Voropayev, S.I., Fernando, H.J.S. & Mitchell, L.A., (1995). On the rate of frazil ice formation in polar regions in the presence of turbulence*. Journal of Physical Oceanography* 25(6):1441-1450.

Wadhams, P., 1986. The ice cover, In Hurdle, B. (ed.): *The Nordic seas*, 211-235. Springer Verlag, New York. pp. 21–86

Wadhams, P. and S. Martin, (1990). Processes determining the bottom topography of multiyear Arctic sea ice. In *Sea Ice Properties and Processes* (eds. S. F. Ackley, W. F. Weeks), Monograph 90-1, US Army Cold Regions Res. & Engng Lab., Hanover, NH., 136-141.

Wadhams P, (2000). *Ice in the ocean*. Gordon and Breach Publishers. pp 351.

Wadhams,P., Wilkinson,J. P., Kaletzky, (2004). A. Sidescan Sonar Imagery of the Winter Marginal Ice Zone Obtained from an AUV *Journal of Atmospheric and Oceanic Technology* 2004 21: 1462-1470

Wadhams (2006)

Wadhams, P., J. P. Wilkinson, and S. D. McPhail (2006), A new view of the underside of Arctic sea ice, *Geophys. Res. Lett.*, *33*, L04501, doi:10.1029/2005GL025131.

Wang, S. D.; Shen, Y. M.; Zheng, Y. H., (2005). Two dimensional numerical simulation for transport and fate of oil spill in seas. Ocean Eng., 32 (13), 1556-1571.

Weeks, W.F., (1998). Growth conditions and the structure and properties of sea ice *Physics of ice-covered seas*: lecture notes from a summer school in Savonlinna, Finland. University of Helsinki, vol. 1:25-104.

Weeks, W. F., and W. D. Hibler. On Sea Ice. Fairbanks: U of Alaska, 2010.

Wilkinson, J. P., P. Wadhams, and N. E. Hughes (2007), Modelling the spread of oil under fast sea ice using three-dimensional multibeam sonar data, *Geophys. Res. Lett.*, 34, L22506, doi:10.1029/2007GL031754.

Wilmes, S., Nicolaus, M., and Bareiss, J. (2009). Satellite Microwave Observations of the Interannual Variability of Snowmelt on Sea Ice in the Southern Ocean. Journal of Geophysical Research-Oceans, 114, C03006, doi: 10.1029/2008JC004919.

Zubov, N. N., *Arctic Ice* (in Russian), 1945. Glavsevmorputi, Moscow, 491 pp. (English translation, U.S. Naval Oceanographic Office, Suitland, Md., 1965.)

ANNEX. ALTERATIONS FROM TASK

There are two alterations to the Task as it is written in the DOW. Originally the plan was to perform experiments with three relevant hydrocarbon products. These were

1. • Gas Condensate: A by-product of gas extraction i.e. the Shtockman field.
2. • Heavy fuel oil: The type of oil that may be spilt should there be a shipping accident and ,
3. • A medium North Sea crude: This is one of the oil types used in the JIP experiments and thus direct

Due to circumstances beyond our control, we were unable to obtain two of these hydrocarbon products. We understand that the combination of global LNG oversupply and higher costs meant that the Shtockman project has been put the project on hold. They were a stakeholder with ACCESS and were to provide gas condensate to us. We could not find another supplier. It was a similar problem with the heavy fuel oil, no supplier could be found. However we are extremely grateful to BP for their help in obtaining the crude oil for both the HSVA experiments as well as the experiments at CRREL. These two crude oil types hold similar properties and are the types of crude oil that one would expect to find in the Arctic should a spill occur.